

# Transport Barriers, Resonance Tori, and Torus-Chaos In a Vector Field With a Neimark-Sacker Bifurcation

Emmanuel Fleurantin, J.D. Mireles James

Department of Mathematics, Florida Atlantic University, 777 Glades Rd, Boca Raton, FL 33431

Email: efleurantin2013@fau.edu, jmirelesjames@fau.edu

## Abstract

We make a detailed numerical study of the dynamics of a three dimensional dissipative vector field exhibiting a Neimark-Sacker bifurcation. Our main goals are to follow the attracting invariant torus born out of this bifurcation to its destruction in subsequent appearance of a chaotic attractor, and also to study the stable/unstable manifolds of the equilibrium solutions which act as separatrices/transport barriers for the system. Computing the periodic orbits – and the stable/unstable manifolds – which make up the resonance torus provides a reliable method for visualization, especially in the regime where the torus is only a  $C^0$  invariant object. Collisions between the stable/unstable manifolds of the periodic orbits signal the destruction of the invariant torus and the onset of chaos.

**Keywords:** Invariant Tori, Neimark-Sacker Bifurcation, Parameterization Method

**AMS Subject Classifications:** 34C45, 37G35, 37M05, 37C55

## 1 Introduction

Tension between two or more natural frequencies in a nonlinear system can give rise to nontrivial motions such as periodic orbits, invariant tori, mode locking, and can even provide a route to chaos. We are interested in the case of a Neimark-Sacker bifurcation [1, 2], where an attracting periodic orbit has a complex conjugate pair of Floquet exponents which crosses the imaginary axis. This results in the loss of stability of the orbit and gives rise to a smooth invariant torus. The period of the orbit and the frequency of the Floquet multipliers provide two internal frequencies, and the interplay between these frequencies determines the evolution of the invariant torus after the bifurcation.

The birth, evolution, and death of invariant tori in dissipative multi-frequency systems is a classical topic and we refer to the classic theoretical works of [3, 4, 5] on dissipative dynamics, the related work of [6, 7, 8, 9] on area and volume preserving systems, and to the numerical study of [10]. The last reference just cited is especially relevant to the present discussion as it introduced the model of the Neimark-Sacker bifurcation further studied in the present work. We refer also to the more recent work of [11, 12] for more complete discussion of hyperbolic invariant tori and the related literature.

---

In this paper we study, from the numerical point of view, the dynamics of a three dimensional dissipative vector field which undergoes a Neimark-Sacker bifurcation giving rise to an attracting invariant torus. We provide detailed computations of the torus as it passes from  $C^k$  to only  $C^0$  regularity – and as its dynamics change from linear to resonant – before it finally breaks up in the birth of a chaotic attractor.

In addition to studying the attracting invariant torus, we examine the embedding of some hyperbolic invariant objects like the stable/unstable manifolds of nearby equilibria and periodic orbits. Accurate computation of hyperbolic invariant objects is critical in the present context as the stable/unstable manifolds of the equilibrium solutions act as transport barriers which form the boundary of the “vortex bubble” which surrounds/contains the attracting invariant torus. Similarly, hyperbolic periodic orbits and their stable/unstable manifolds play a critical role in describing the attracting torus and its dynamics in the resonant/low regularity regime.

More precisely, a resonant torus is further decomposed into one or more attracting periodic orbits and one or more hyperbolic periodic orbits with one stable and one unstable direction. The unstable manifold of the hyperbolic orbit is fully absorbed into the basin of attraction of the stable periodic orbit. The union of the stable and hyperbolic periodic orbits with the unstable manifolds give the resonant invariant torus. Then numerical integration of any initial condition in the basin of attraction of the torus will always converge to the attracting periodic orbit. To accurately visualize the resonant torus we must compute also the unstable periodic orbit and its invariant manifold.

We use the parameterization method of Cabré, Fontich, and de la Llave [13, 14, 15], to compute the stable/unstable manifolds of the equilibrium solutions. The parameterization method provides a functional analytic framework for studying invariant manifolds, and in particular leads to methods for high order polynomial approximation. The periodic orbits on the other hand are computed using Newton’s method in an appropriate Poincaré section. Their stable/unstable manifolds are computed using the standard linear approximation by eigenvectors of the monodromy. Integrating the section data provides a much more accurate method for three dimensional visualization of the resonant tori than obtained by simply integrating initial conditions in the basin of the attractor which, as just mentioned, converge to the attracting orbit.

The remainder of the paper is organized as follows. In the next two subsections we first describe the three dimensional model under consideration, and then discuss briefly some related literature. In Section 2 we study the local stable/unstable manifolds of the equilibrium points using the parameterization method. The method is reviewed and the appropriate recursion relations (the *homological equations*) are derived. We globalize the local invariant manifolds obtained using the parameterization method in order to get a better picture of the structure of the attracting set. In Section 3 we refine this picture by studying an appropriate Poincaré section. We conclude the paper in Section 4 with a few conclusions and observations.

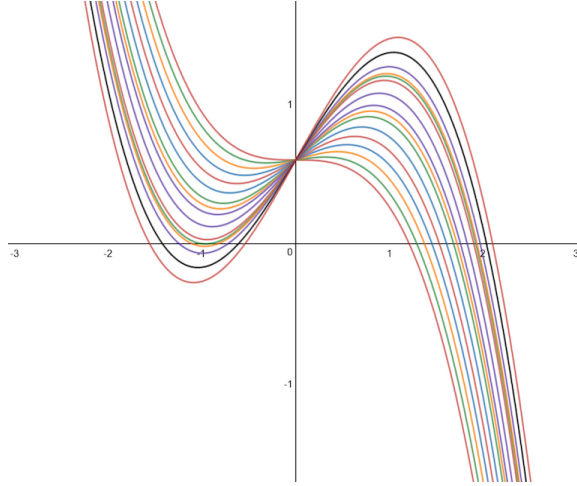


Figure 1: Graph of  $g(z) = \tau + \alpha z - \frac{z^3}{3}$  for different parameter values of  $\alpha$  and fixed  $\tau = 0.6$ .

## 1.1 A simple model of a vortex

We consider the dynamics generated by the 3D vector field

$$f(x, y, z) = \begin{pmatrix} (z - \beta)x - \delta y \\ \delta x + (z - \beta)y \\ \tau + \alpha z - \frac{z^3}{3} - (x^2 + y^2)(1 + \varepsilon z) + \zeta z x^3 \end{pmatrix}, \quad (1)$$

where  $\varepsilon = 0.25$ ,  $\tau = 0.6$ ,  $\delta = 3.5$ ,  $\beta = 0.7$ ,  $\zeta = 0.1$ . We treat  $\alpha > 0$  as a bifurcation parameter. The system was introduced by Langford in [10] as a truncation to second order of the normal form for a Hopf bifurcation, with the inclusion of third order terms which break the axial symmetry. The symmetry breaking is important for describing the dynamics following a generic bifurcation.

We begin with some elementary observations which inform the numerical study to follow. Note that the  $z$ -axis is an invariant sub-system as  $x = y = 0$  implies that  $x' = y' = 0$ . The dynamics on the  $z$ -axis are governed by the scalar differential equation

$$z' = \tau + \alpha z - \frac{z^3}{3} =: g(z).$$

The function  $g(z)$  is illustrated in Figure 1, and since  $\tau > 0$ ,  $g$  has one, two, or three zeros depending on the parameter  $\alpha$ . Moreover, equilibria of  $f$  occur at  $(0, 0, z_*)$  where  $z_*$  is a zero of  $g$ . Observe that for large positive  $z$ ,  $z' < 0$ . While for large negative  $z$ ,  $z' > 0$ . That is, the field tends to diminish the  $z$  value of a phase point whose  $z$  value happens to be large.

For all  $\alpha \in \mathbb{R}$  the system has at least one equilibrium solution, which we denote by  $p_0 \in \mathbb{R}^3$ . This equilibrium has one stable eigenvalue, whose eigenvector coincides with the  $z$ -axis. The remaining eigenvalues are complex conjugate unstable. At  $\alpha_* = 0.9321697517861$  there is a saddle node bifurcation giving rise to a new pair of equilibrium points  $p_1, p_2 \in \mathbb{R}^3$ . These equilibria persist for all  $\alpha > \alpha_*$ . One of these points is fully stable, with three

---

eigenvalues having negative real parts, and we denote this stable equilibrium by  $p_2 \in \mathbb{R}^3$ . The other point, which we denote by  $p_1 \in \mathbb{R}^3$ , is a saddle-focus with a pair of complex conjugate stable eigenvalues and one real unstable eigenvalue. The unstable eigenvector again coincides with the  $z$ -axis. Indeed, since the  $z$ -axis is invariant, the stable manifold of  $p_0$  and the unstable manifold of  $p_1$  coincide, and are contained in the  $z$ -axis. This intersection is not transverse, and is rather forced by the rotational symmetry of the problem.

Now consider the plane  $z = \beta$ , and note that when the field is projected onto this plane we obtain a pure rotation. The plane is however not invariant, as  $z'$  does not vanish there. Nevertheless there is a periodic orbit  $\gamma$  in the plane, which occurs where  $z' = 0$  in the  $z = \beta$  plane. This periodic orbit, and the invariant  $z$  axis organize the dynamics of the system. The vector field along with the periodic orbit and the dynamics on the  $z$ -axis are illustrated in the left frame of Figure 2.

As we will see below, the periodic orbit  $\gamma$  has a pair of complex conjugate Floquet exponents, hence solutions of the differential equation tend to circulate around  $\gamma$ . The orbit may be either attracting or repelling depending on the value of  $\alpha$ . This circulation about the periodic orbit is a dominant feature of the dynamics.

Further insight is obtained by numerically integrating some trajectories for a long time (phase space sampling) and disregarding the transient portion of the orbit, as was done in the work of Langford [10]. We provide, for the sake of completeness, the results of a few such simulations. For example, in Figure 3 we see the orbit of an arbitrary initial condition advected for about one hundred time units. After discarding the transients we see that the system seems to have a “torus-like” attractor for many parameter values. The left and right frames of Figure 3 illustrate the apparent attractor for  $\alpha = 0.8$  and  $\alpha = 0.95$  – the “classic value” of  $\alpha$  – respectively. The periodic orbit runs through the center of the torus. The saddle focus points  $p_0$  and  $p_1$  are at the top and bottom.

## 1.2 Some remarks on the literature

Roughly speaking, the dynamics described above suggests the system as a toy model for dissipative vortex dynamics, or for a rotating viscous fluid. There is a rich literature on the dynamics of vortex bubbles, and the interested reader might consult the works of [9, 16, 17, 18, 19] for a more thorough discussion of the literature. We remark that the torus bifurcations seen in the Aizawa system are similar to those seen in the piecewise linear electronic circuit of [20], the commodity distribution model of [21], and the mechanical oscillators of [22, 23] to name only a few. Resonant invariant tori and torus-chaos are discussed much more generally in [5, 24] and the references found therein.

One further remark is in order. The system given by Equation (1) has been called *the Aizawa system* by some researchers, and is the subject of some other recent work on visualization. For example researchers interested in computer animation [25], three dimensional printing [26], and even the graphic arts [27] have made interesting studies and use this name for the equations. This seems however to be a misnomer, as the equations seem not to have appeared in the works of Yoji Aizawa. A more appropriate name would appear to be *the Langford system*, due to the fact that, as already mentioned above, the system was proposed in [10].

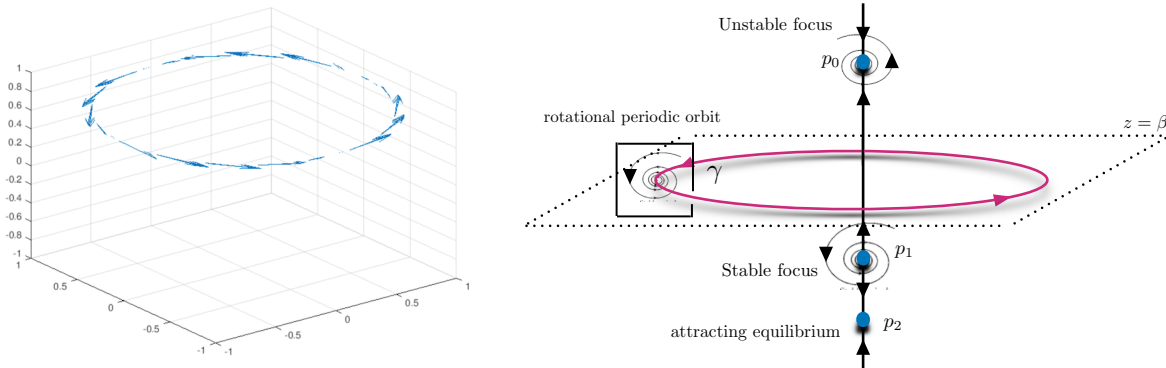


Figure 2: Phase space geography of the Aizawa system: the main features of the system are the invariance of the  $z$ -axis, the rotation in the  $z = \beta$  plane leading to a periodic orbit, and the unstable saddle focus at  $p_0$ . The periodic orbit  $\gamma$  is located near (but does not sit on) the  $z = \beta$  plane. The periodic orbit has complex conjugate Floquet multipliers which are stable for small  $\alpha$  but which later cross the unit circle, losing stability in a Neimark-Sacker bifurcation. For some  $\alpha$  values there are an additional pair of equilibria  $p_1$  – stable focus and  $p_2$  – attracting point. This situation is illustrated in the schematic on the right. Left: The phase portrait of the vector field along the periodic orbit.

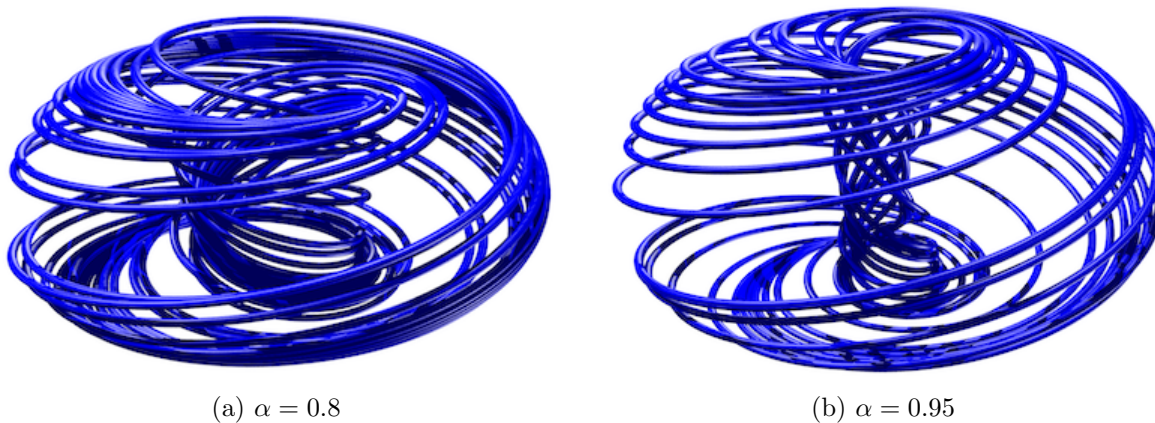


Figure 3: Numerical integration of the Aizawa system. For many parameter values of  $\alpha$  the system appears to have an attractor with torus-like dynamics (product of two circles). This is caused by circulation due to the complex conjugate Floquet exponents of the periodic orbit, and generates what we refer to as a vortex.

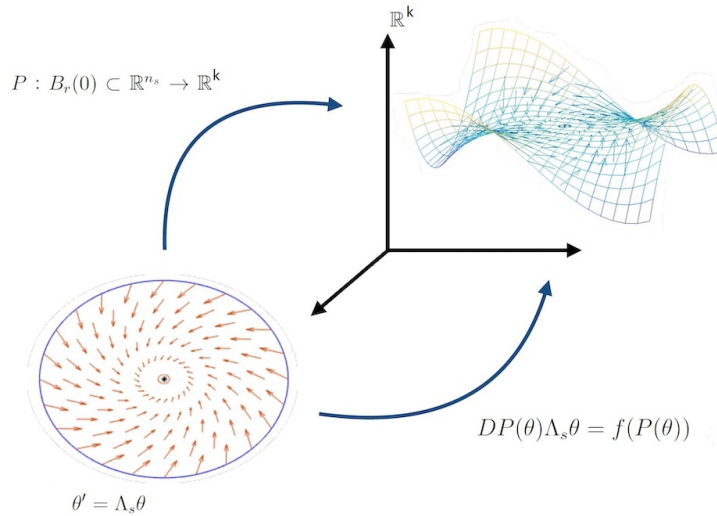


Figure 4: Geometry of the parameterization method: the push forward of the linear vector field  $\Lambda_s \theta$  by  $P$  is equal to the given vector field  $f$  restricted to the image of  $P$ . Then the dynamics on the image of  $P$  are conjugate to the linear dynamics generated by  $\Lambda_s \theta$ .

## 2 The Parameterization Method

The parameterization method is a general functional analytic framework for studying invariant manifolds of discrete and continuous time dynamical systems, first developed in [13, 14, 15] for the context of the stable/unstable manifold associated to a fixed point of non-linear mapping on a Banach space, and later extended in [28, 29, 30] for studying whiskered tori. There is a thriving literature devoted to computational applications of the parameterization method, and the interested reader may want to consult [11, 12, 31, 32, 33, 34, 35, 36, 37, 38, 39, 40, 41, 42, 43], though the list is far from being exhaustive. Much more complete discussion of the literature is found in the book [44].

This section reviews as much of the method used in the present work. First a little notation. Let field  $f : \mathbb{R}^k \rightarrow \mathbb{R}^k$  be a real analytic vector field and consider a hyperbolic equilibrium point  $\bar{x} \in \mathbb{R}^k$ . That is suppose that  $f(\bar{x}) = 0$  and that  $Df(\bar{x})$  has no eigenvalues on the imaginary axis. Then there are  $k_s, k_u \in \mathbb{N}$  with  $k_s + k_u = k$  so that  $Df(\bar{x})$  has  $k_s$  stable eigenvalues and  $k_u$  unstable eigenvalues (counted with multiplicity). We label the eigenvalues as  $\lambda_1^s, \dots, \lambda_{k_s}^s$  for the stable, and  $\lambda_1^u, \dots, \lambda_{k_u}^u$  for the unstable. We order the eigenvalues so that

$$\text{real}(\lambda_1^s) \leq \dots \leq \text{real}(\lambda_{k_s}^s) < 0 < \text{real}(\lambda_1^u) \leq \dots \text{real}(\lambda_{k_u}^u).$$

The discussion is somewhat simplified if we suppose that  $Df(\bar{x})$  is diagonalizable. Then there are linearly independent eigenvectors  $\xi_1^u, \dots, \xi_{k_u}^u$  and  $\xi_1^s, \dots, \xi_{k_s}^s \in \mathbb{R}^k$  associated with the unstable and stable eigenvalues respectively.

---

## 2.1 Invariance equation

We seek an  $r > 0$  and a smooth surjective map  $P : B_r(0) \subset \mathbb{R}^{k_s} \rightarrow \mathbb{R}^k$  satisfying the first order system of partial differential equations

$$\lambda_1^s \theta_1 \frac{\partial}{\partial \theta_1} P(\theta_1, \dots, \theta_{k_s}) + \dots + \lambda_{k_s}^s \theta_{k_s} \frac{\partial}{\partial \theta_{k_s}} P(\theta_1, \dots, \theta_{k_s}) = f(P(\theta_1, \dots, \theta_{k_s})), \quad (2)$$

subject to the first order constraints

$$P(0, \dots, 0) = \hat{p}, \quad \text{and} \quad \frac{\partial}{\partial \theta_j} P = \xi_j^s. \quad (3)$$

To explain the geometric meaning of Equation (2), let

$$\Lambda_s = \begin{pmatrix} \lambda_1 & \dots & 0 \\ \vdots & \ddots & \vdots \\ 0 & \dots & \lambda_{k_s} \end{pmatrix},$$

and  $\theta = (\theta_1, \dots, \theta_{k_s}) \in B_r(0) \subset \mathbb{R}^{k_s}$ . The invariance equation becomes

$$DP(\theta)\Lambda_s\theta = f(P(\theta)),$$

and  $P$  has the following property: that the push forward of the linear vector field  $\Lambda_s\theta$  is equal to the vector field  $f$  when restricted to the image of  $P$ . Since the vector fields are equal, they generate the same dynamics. But the dynamics generated on  $\mathbb{R}^{k_s}$  by  $\Lambda_s\theta$  are completely understood: all orbits converge exponentially to the origin. The situation is illustrated in Figure 4.

More is true. Denote by  $\phi: \mathbb{R}^k \times \mathbb{R} \rightarrow \mathbb{R}^k$  the flow generated by  $f$ . The flow generated by  $\Lambda_s\theta$  is given by

$$L(\theta, t) = e^{\Lambda_s t} \theta.$$

Then  $P$  satisfies Equation (2), if and only if

$$\phi(P(\theta), t) = P(e^{\Lambda_s t} \theta), \quad (4)$$

for all  $t \geq 0$ . This flow conjugacy is illustrated in Figure 5. Combining the flow conjugacy with the first order constraints of Equation (3) we have that  $P$  is a chart map for the local stable manifold attached to the equilibrium solution  $\hat{p} \in \mathbb{R}^k$ .

Elementary proofs of the claims above are found in any of the references [37, 44, 45]. Moreover, replacing the stable by the unstable eigenvalues and eigenvectors in the discussion above and reversing time, the entire discussion carries through for the unstable manifold.

## 2.2 Formal series solution of Equation (2)

Let  $\hat{p} \in \mathbb{R}^3$  be an equilibrium solution of Equation (1) and suppose that  $\lambda_1, \lambda_2 \in \mathbb{C}$  are a pair of stable (or unstable) eigenvalues and suppose that  $\lambda_3$  has the opposite stability. Let

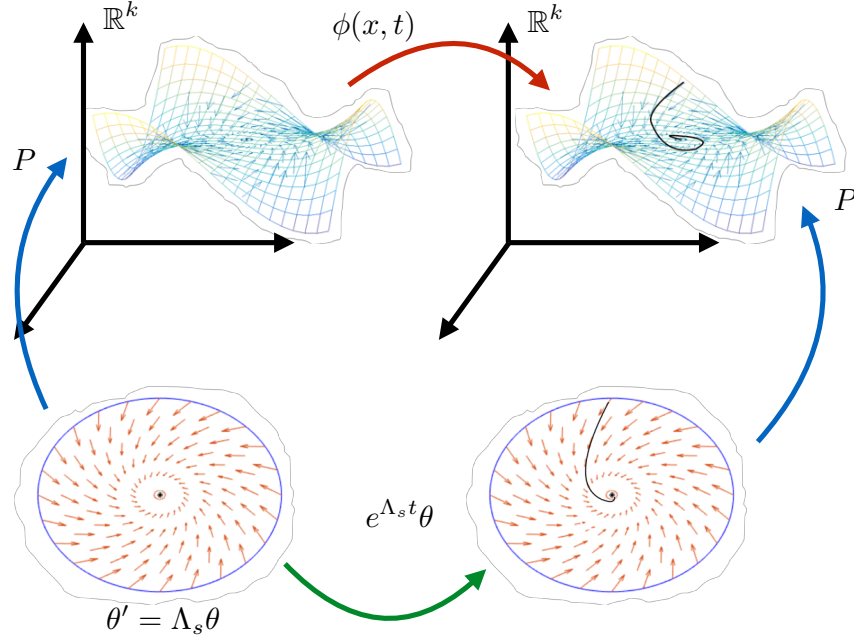


Figure 5: Flow conjugacy: a mapping  $P$  satisfying the invariance equation (2) has that the diagram above commutes.

$\xi_1, \xi_2 \in \mathbb{C}^3$  be an associated pair of linearly independent eigenvectors. Since the field is analytic, we look for an analytic parameterization

$$P(\theta_1, \theta_2) = \sum_{m=0}^{\infty} \sum_{n=0}^{\infty} \begin{pmatrix} p_{mn}^1 \\ p_{mn}^2 \\ p_{mn}^3 \end{pmatrix} \theta_1^m \theta_2^n,$$

having that

$$\lambda_1 \theta_1 \frac{\partial}{\partial \theta_1} P(\theta_1, \theta_2) + \lambda_2 \theta_2 \frac{\partial}{\partial \theta_2} P(\theta_1, \theta_2) = f(P(\theta_1, \theta_2)).$$

Here  $p_{mn}^j \in \mathbb{C}$  for all  $j = 1, 2, 3$ . Imposing the linear constraints of Equation (3) gives that  $p_{00} = \hat{p}$ ,  $p_{10} = \xi_1$  and  $p_{01} = \xi_2$ . Observe that

$$\lambda_1 \theta_1 \frac{\partial}{\partial \theta_1} P(\theta_1, \theta_2) + \lambda_2 \theta_2 \frac{\partial}{\partial \theta_2} P(\theta_1, \theta_2) = \sum_{m=0}^{\infty} \sum_{n=0}^{\infty} (m\lambda_1 + n\lambda_2) p_{mn} \theta_1^m \theta_2^n,$$

on the level of power series.

Computing the composition on the level of power series is more delicate and we introduce some helpful notation. We write

$$P_j(\theta_1, \theta_2) = \sum_{m=0}^{\infty} \sum_{n=0}^{\infty} p_{mn}^j \theta_1^m \theta_2^n,$$

for  $j = 1, 2, 3$  to denote the component power series. The field contains the nonlinear terms  $zx, zy, z^3, x^2z, y^2z$ , and  $zx^3$ . Computing the power series for  $f \circ P$  requires computing the



corresponding power series products. To this end define the components of the two variable Cauchy products

$$\begin{aligned}
(p^3 * p^1)_{mn} &= \sum_{j=0}^m \sum_{k=0}^n p_{(m-j)(n-k)}^3 p_{jk}^1 \\
(p^3 * p^2)_{mn} &= \sum_{j=0}^m \sum_{k=0}^n p_{(m-j)(n-k)}^3 p_{jk}^2 \\
(p^3 * p^3 * p^3)_{mn} &= \sum_{i=0}^m \sum_{j=0}^i \sum_{k=0}^n \sum_{l=0}^k p_{(m-i)(n-k)}^3 p_{(i-j)(k-l)}^3 p_{jl}^3, \\
(p^1 * p^1 * p^3)_{mn} &= \sum_{i=0}^m \sum_{j=0}^i \sum_{k=0}^n \sum_{l=0}^k p_{(m-i)(n-k)}^1 p_{(i-j)(k-l)}^1 p_{jl}^3, \\
(p^2 * p^2 * p^3)_{mn} &= \sum_{i=0}^m \sum_{j=0}^i \sum_{k=0}^n \sum_{l=0}^k p_{(m-i)(n-k)}^2 p_{(i-j)(k-l)}^2 p_{jl}^3,
\end{aligned}$$

and

$$(p^3 * p^1 * p^1 * p^1)_{mn} = \sum_{i_1=0}^m \sum_{i_2=0}^{i_1} \sum_{i_3=0}^{i_2} \sum_{k_1=0}^n \sum_{k_2=0}^{k_1} \sum_{k_3=0}^{k_2} p_{(m-i_1)(n-k_1)}^3 p_{(i_1-i_2)(k_1-k_2)}^1 p_{(i_2-i_3)(k_2-k_3)}^1 p_{i_3 k_3}^1.$$

Then

$$\begin{aligned}
(P_3 \cdot P_1)(\theta_1, \theta_2) &= \sum_{m=0}^{\infty} \sum_{n=0}^{\infty} (p^3 * p^1)_{mn} \theta_1^m \theta_n^2, \\
(P_3 \cdot P_2)(\theta_1, \theta_2) &= \sum_{m=0}^{\infty} \sum_{n=0}^{\infty} (p^3 * p^2)_{mn} \theta_1^m \theta_n^2, \\
(P_3 \cdot P_3 \cdot P_3)(\theta_1, \theta_2) &= \sum_{m=0}^{\infty} \sum_{n=0}^{\infty} (p^3 * p^3 * p^3)_{mn} \theta_1^m \theta_n^2, \\
(P_1 \cdot P_1 \cdot P_3)(\theta_1, \theta_2) &= \sum_{m=0}^{\infty} \sum_{n=0}^{\infty} (p^1 * p^1 * p^3)_{mn} \theta_1^m \theta_n^2, \\
(P_2 \cdot P_2 \cdot P_3)(\theta_1, \theta_2) &= \sum_{m=0}^{\infty} \sum_{n=0}^{\infty} (p^2 * p^2 * p^3)_{mn} \theta_1^m \theta_n^2,
\end{aligned}$$

and

$$(P_3 \cdot P_1 \cdot P_1 \cdot P_1)(\theta_1, \theta_2) = \sum_{m=0}^{\infty} \sum_{n=0}^{\infty} (p^3 * p^1 * p^1 * p^1)_{mn} \theta_1^m \theta_n^2.$$

Plugging these power series expansions into the invariance equation (2) and matching like powers of  $\theta_1$  and  $\theta_2$  gives

$$(m\lambda_1 + n\lambda_1) \begin{bmatrix} p_{mn}^1 \\ p_{mn}^2 \\ p_{mn}^3 \end{bmatrix} = \tag{5}$$

$$\left[ \begin{array}{c} (p^3 * p^1)_{mn} - \beta p_{mn}^1 - \delta p_{mn}^2 \\ (p^3 * p^2)_{mn} - \beta p_{mn}^2 + \delta p_{mn}^3 \\ \alpha p_{mn}^3 - \frac{1}{3}(p^3 * p^3 * p^3)_{mn} - (p^1 * p^1)_{mn} - (p^2 * p^2)_{mn} - \varepsilon(p^1 * p^1 * p^3)_{mn} - \varepsilon(p^2 * p^2 * p^3)_{mn} + \zeta(p^1 * p^3 * p^3 * p^3)_{mn} \end{array} \right],$$

for  $m + n \geq 2$ .

Now we would like to separate terms depending on  $p_{mn}$  from lower order terms. Let us consider the first component in somewhat more detail. Observe that

$$(p^3 * p^1)_{mn} = p_{00}^3 p_{mn}^1 + p_{00}^1 p_{mn}^3 + (p^3 \hat{*} p^1)_{mn},$$

where

$$(p^3 \hat{*} p^1)_{mn} = \sum_{j=0}^m \sum_{k=0}^n \hat{\delta}_{jk}^{mn} p_{(m-j)(n-k)}^3 p_{jk}^1,$$

and

$$\hat{\delta}_{jk}^{mn} = \begin{cases} 0 & \text{if } j = k = 0 \\ 0 & \text{if } j = m \text{ and } k = n \\ 1 & \text{otherwise} \end{cases}.$$

The point is that  $(p^3 \hat{*} p^1)_{mn}$  is precisely the sum left when terms containing  $p_{mn}$  are extracted from the Cauchy product. In fact, letting

$$g(x, z) = xz,$$

we have that

$$(g \circ P)_{mn} = \nabla g(p_{00}^1, p_{00}^3) \begin{bmatrix} p_{mn}^1 \\ p_{mn}^3 \end{bmatrix} + (p^1 \hat{*} p^3)_{mn}.$$

Then the first component of Equation (5) becomes

$$(m\lambda_1 + n\lambda_2)p_{mn}^1 = \nabla g(p_{00}^1, p_{00}^3) \begin{bmatrix} p_{mn}^1 \\ p_{mn}^3 \end{bmatrix} + (p^1 \hat{*} p^3)_{mn} - \beta p_{mn}^1 - \delta p_{mn}^2.$$

Isolating terms of order  $(m, n)$  on the left and lower order terms on the right gives

$$\nabla g(p_{00}^1, p_{00}^3) \begin{bmatrix} p_{mn}^1 \\ p_{mn}^3 \end{bmatrix} - \beta p_{mn}^1 - \delta p_{mn}^2 - (m\lambda_1 + n\lambda_2)p_{mn}^1 = -(p^1 \hat{*} p^3)_{mn},$$

which is linear in  $p_{mn}^1$ . Comparing the right hand side in the equation above with the vector field  $f$ , and recalling that  $\hat{p} = p_{00}$ , we see that

$$\nabla g(p_{00}^1, p_{00}^3) \begin{bmatrix} p_{mn}^1 \\ p_{mn}^3 \end{bmatrix} - \beta p_{mn}^1 - \delta p_{mn}^2 = \nabla f_1(\hat{p}) \begin{bmatrix} p_{mn}^1 \\ p_{mn}^3 \end{bmatrix}.$$

Combining the equation above with a nearly identical computation for the second component, and a somewhat lengthier computation for the third component, and noting that

$$Df(\hat{p})p_{mn} = \begin{bmatrix} \nabla f_1(\hat{p}) \\ \nabla f_2(\hat{p}) \\ \nabla f_3(\hat{p}) \end{bmatrix},$$

we obtain the expansion

$$(f \circ P)_{mn} = Df(\hat{p})p_{mn} + \left[ \begin{array}{c} (p^3 \hat{*} p^1)_{mn} \\ (p^3 \hat{*} p^2)_{mn} \\ -\frac{1}{3}(p^3 \hat{*} p^3 \hat{*} p^3)_{mn} - (p^1 \hat{*} p^1)_{mn} - (p^2 \hat{*} p^2)_{mn} - \varepsilon(p^1 \hat{*} p^1 \hat{*} p^3)_{mn} - \varepsilon(p^2 \hat{*} p^2 \hat{*} p^3)_{mn} + \zeta(p^1 \hat{*} p^3 \hat{*} p^3 \hat{*} p^3)_{mn} \end{array} \right].$$

Plugging this expansion into Equation (5) gives

$$(m\lambda_1 + n\lambda_2)p_{mn} = Df(\hat{p})p_{mn} + \left[ \begin{array}{c} (p^3 \hat{*} p^1)_{mn} \\ (p^3 \hat{*} p^2)_{mn} \\ -\frac{1}{3}(p^3 \hat{*} p^3 \hat{*} p^3)_{mn} - (p^1 \hat{*} p^1)_{mn} - (p^2 \hat{*} p^2)_{mn} - \varepsilon(p^1 \hat{*} p^1 \hat{*} p^3)_{mn} - \varepsilon(p^2 \hat{*} p^2 \hat{*} p^3)_{mn} + \zeta(p^1 \hat{*} p^3 \hat{*} p^3 \hat{*} p^3)_{mn} \end{array} \right],$$

and by isolating terms depending on  $p_{mn}$  on the left and lower order terms on the right, we obtain the linear *homological equations*

$$[Df(\hat{p}) - (m\lambda_1 + n\lambda_2)\text{Id}]p_{mn} = s_{mn}, \quad (6)$$

for  $p_{mn}$ , where

$$s_{mn} = \begin{pmatrix} s_{mn}^1 \\ s_{mn}^2 \\ s_{mn}^3 \end{pmatrix},$$

with

$$\begin{aligned} s_{mn}^1 &= -(p^3 \hat{*} p^1)_{mn}, \\ s_{mn}^2 &= -(p^3 \hat{*} p^2)_{mn}, \end{aligned}$$

and

$$s_{mn}^3 = \frac{1}{3}(p^3 \hat{*} p^3 \hat{*} p^3)_{mn} + (p^1 \hat{*} p^1)_{mn} + (p^2 \hat{*} p^2)_{mn} + \varepsilon(p^1 \hat{*} p^1 \hat{*} p^3)_{mn} + \varepsilon(p^2 \hat{*} p^2 \hat{*} p^3)_{mn} - \zeta(p^1 \hat{*} p^1 \hat{*} p^1 \hat{*} p^3)_{mn}.$$

We have the following observations.

- The matrix acting on  $p_{mn}$  is the characteristic matrix for the differential at  $\hat{p}$ . Then the equation is uniquely solvable at order  $(m, n)$  if  $m\lambda_1 + n\lambda_2$  is not an eigenvalue.
- Since  $\lambda_3$  has the opposite stability of  $\lambda_1, \lambda_2$ , we obtain the *non-resonance condition*

$$m\lambda_1 + n\lambda_2 \neq \lambda_j, \quad j = 1, 2.$$

If the non-resonance conditions are satisfied for all  $m, n \in \mathbb{N}$  with  $m + n \geq 2$ , then the formal series solution of Equation (2) is formally well defined to all orders.

- If  $\lambda_2 = \overline{\lambda_1}$ , that is if we consider the complex conjugate case, then there is no possibility of a resonance and we can compute the power series coefficients of the parameterization to any desired finite order.

- When  $\lambda_1, \lambda_2$  are complex conjugates, the coefficients of  $P$  have the symmetry  $\overline{p_{nm}} = p_{mn}$  for all  $m + n \geq 2$ . This is seen by taking complex conjugates of both sides of the homological equation, and using the fact that  $Df(\hat{p})$  is a real matrix.

Since  $\hat{p}$  is real, choosing complex conjugate eigenvectors  $\xi_2 = \overline{\xi_1}$  enforces the symmetry to all orders. The power series solution  $P$  has complex coefficients, but we obtain the real image of  $P$  by taking complex conjugate variables. That is, we define for the real parameters  $s_1, s_2$  the function

$$\hat{P}(s_1, s_2) = P(s_1 + is_2, s_1 - is_2),$$

which parameterizes the real stable/unstable manifold.

## 2.3 Numerical considerations

The homological equations derived in the previous section allow us to recursively compute the power series coefficients of the stable/unstable manifold parameterization  $P$  to any desired order  $m + n = N$ . The coefficients are uniquely determined up to the choice of the scaling of the eigenvectors. In practical applications we have to decide how to answer the following questions:

- To what order  $N$  will we compute the approximate parameterization?
- What scale to choose for the eigenvectors?
- On what domain do we to restrict the polynomial  $P^N$ ?

In practice we proceed as follows. First we choose a convenient value for  $N$ , based on how long we want to let the computations run. Then, we always restrict  $P$  to the unit disk for the sake of numerical stability. Finally, we choose the eigenvector scaling so that the last coefficients, the coefficients of order  $N$ , are smaller than some prescribed tolerance. A good empirical rule of thumb is that the truncation error is roughly the same magnitude as the  $N$ -th order coefficients.

In practice we can prescribe the size of the  $N$ -th order terms as soon as we know the exponential decay rate of the coefficients. In the next section we describe the relationship between the scale of the eigenvectors and the exponential decay rate.

### 2.3.1 Rescaling the eigenvectors

In Section 2.2 we saw that the power series coefficients of the parameterization are uniquely determined up to the choice of the eigenvector. Since the eigenvectors are unique up to the choice of length, we have that the length determines uniquely the coefficients. In fact the effect of rescaling the eigenvectors is made completely explicit as follows. The material in this section is discussed in greater detail in [35].

Suppose that

$$P(\theta_1, \theta_2) = \sum_{m=0}^{\infty} \sum_{n=0}^{\infty} p_{mn} \theta_1^m \theta_2^n,$$

is the formal solution of the invariance equation

$$DP(\theta)\Lambda\theta = f(P(\theta)),$$

subject to the constraints

$$p_{00} = \hat{p}, \quad p_{10} = \xi_1, \quad \text{and} \quad p_{01} = \xi_2,$$

where  $\|\xi_1\| = \|\xi_2\| = 1$ . Assuming that  $P$  is bounded and analytic on the complex poly-disk with radii  $R_1, R_2 > 0$ , there is a  $C > 0$  so that

$$|p_{mn}| \leq \frac{C}{R_1^m R_2^n},$$

by the Cauchy estimates.

Now choose non-zero  $s_1, s_2 \in \mathbb{R}$  and define the rescaled eigenvectors

$$\eta_1 = s_1 \xi_1, \quad \text{and} \quad \eta_2 = s_2 \xi_2.$$

We claim that the parameterization associated with these eigenvectors is given by

$$Q(\theta_1, \theta_2) = \sum_{m=0}^{\infty} \sum_{n=0}^{\infty} q_{mn} \theta_1^m \theta_2^n,$$

where

$$q_{mn} = s_1^m s_2^n p_{mn}. \tag{7}$$

The above equality is a consequence of the following observation. We know that:

$$\begin{aligned} Q(\theta_1, \theta_2) &= \sum_{m=0}^{\infty} \sum_{n=0}^{\infty} q_{mn} \theta_1^m \theta_2^n \\ &= \sum_{m=0}^{\infty} \sum_{n=0}^{\infty} s_1^m s_2^n p_{mn} \theta_1^m \theta_2^n \\ &= \sum_{m=0}^{\infty} \sum_{n=0}^{\infty} p_{mn} (s_1 \theta_1)^m (s_2 \theta_2)^n \\ &= P(s_1 \theta_1, s_2 \theta_2) \end{aligned}$$

Then

$$Q(0, 0) = P(0, 0) = \hat{p},$$

$$\frac{\partial}{\partial \theta_1} Q(0, 0) = s_1 \frac{\partial}{\partial \theta_1} P(0, 0) = s_1 \xi_1 = \eta_1, \quad \text{and} \quad \frac{\partial}{\partial \theta_2} Q(0, 0) = s_2 \frac{\partial}{\partial \theta_2} P(0, 0) = s_2 \xi_2 = \eta_2.$$

Then  $Q$  satisfies the first order constraints of the parameterization method. Now, letting  $\tilde{\theta}_1 = s_1\theta_1$ ,  $\tilde{\theta}_2 = s_2\theta_2$  and  $\tilde{\theta} = (\tilde{\theta}_1, \tilde{\theta}_2)$ , we see that

$$\begin{aligned}
DQ(\theta)\Lambda\theta &= DP(s_1\theta_1, s_2\theta_2)\Lambda\theta \\
&= s_1\lambda_2\theta_1\frac{\partial}{\partial\theta_1}P(s_1\theta_1, s_2\theta_2) + s_2\lambda_2\theta_2\frac{\partial}{\partial\theta_2}P(s_1\theta_1, s_2\theta_2) \\
&= DP\left(\tilde{\theta}\right)\Lambda\tilde{\theta} \\
&= f\left(P\left(\tilde{\theta}\right)\right) \\
&= f(P(s_1\theta_1, s_2\theta_2)) \\
&= f(Q(\theta)),
\end{aligned}$$

and  $Q$  is a solution of the invariance equation.

So,  $Q$  is the parameterization satisfying the first order constraints for the rescaled eigenvectors and we have the new exponential decay estimate

$$\begin{aligned}
|q_{mn}| &= |s_1^m s_2^n p_{mn}| \\
&\leq s_1^m s_2^n \frac{C}{R_1^m R_2^n} \\
&\leq \frac{C}{\left(\frac{R_1}{s_1}\right)^m \left(\frac{R_2}{s_2}\right)^n}.
\end{aligned}$$

These observations lead to a practical algorithm as follows. First we compute the parameterization  $P$  with some arbitrary choice of eigenvector scaling (perhaps scaled to length one). Then we solve the homological equations to some order  $N_0$  using this scaling, and compute  $C$ ,  $R_1$  and  $R_2$  using an exponential best fit. Suppose that  $\varepsilon_0 > 0$  is the desired tolerance, that is the desired size of the order  $N \geq N_0$  coefficients. Then we choose  $s_1$  and  $s_2$  so that

$$\frac{C}{\left(\frac{R_1}{s_1}\right)^N \left(\frac{R_2}{s_2}\right)^N} \leq \varepsilon_0.$$

Finally we recompute the coefficients  $q_{mn}$  for  $2 \leq m + n \leq N$ . The rescaled coefficients could be computed from the old coefficients using the formula of Equation (7). In practice however better results are obtained by recomputing the coefficients  $q_{mn}$  from scratch via the homological equations.

We remark that in the case of complex conjugate eigenvalues we want the eigenvectors to be complex conjugates. Assuming that  $\xi_2 = \bar{\xi}_1$  we take  $s_1 = s_2 \in \mathbb{R}$  so that  $\eta_2 = \bar{\eta}_1$ . Also note that by choosing our domain to be the unit poly-disk, we have that  $R_1 = R_2 = 1$ , further simplifying the analysis.

### 2.3.2 A-posteriori error

Once we have chosen the polynomial order  $N$  and the scaling of the eigenvectors, that is once we have uniquely specified our parameterization to order  $N$ , we would like a convenient

measure of the truncation error. As mentioned above, a good heuristic indicator is that the error is roughly the size of the highest order coefficients (assuming we take the unit disk as the domain of our approximate parameterization). In this section we discuss a more quantitative indicator.

We remark that there exist methods of a-posteriori error analysis for the parameterization method, which – when taken to their logical conclusion – lead to mathematically rigorous computer assisted error bounds on the truncation errors. The interested reader will find fuller discussion and more references to the literature in [15, 35, 36, 44, 45, 46] and discussion of related techniques in [47, 48, 49].

The analysis in the present work is qualitative and we don't require the full power of mathematically rigorous error bounds. Instead we employ an error indicator inspired by the fact that the parameterization satisfies the flow invariance property given in Equation (4). We choose  $T \neq 0$ , and a partition of the interval  $[0, 2\pi]$  into  $K$  angles,  $\alpha_j = 2\pi j / (K + 1)$ , for  $0 \leq j \leq K$ . Since we are interested in the case of complex conjugate eigenvalues  $\lambda, \bar{\lambda} \in \mathbb{C}$ , we define complex conjugate parameters

$$\theta_j = (\theta_1^j + i\theta_2^j, \theta_1^j - i\theta_2^j) = (\cos(\alpha_j) + i \sin(\alpha_j), \cos(\alpha_j) - i \sin(\alpha_j)),$$

and the linear mapping

$$e^{\Lambda T} = \begin{pmatrix} e^{\lambda T} & 0 \\ 0 & e^{\bar{\lambda} T} \end{pmatrix}.$$

which maps complex conjugate inputs to complex conjugate outputs. The a-posteriori indicator is

$$\text{Error}_{\text{conj}}(N, T) = \max_{0 \leq j \leq K} \left\| \phi(P^N(\theta_j), T) - P^N(e^{\Lambda T} \theta_j) \right\|.$$

Here  $T > 0$  if the complex conjugate eigenvalues  $\lambda, \bar{\lambda}$  are stable and  $T < 0$  if they are unstable. In practice the flow map  $\phi(x, t)$  will be evaluated using a numerical integration scheme, and the accuracy of the indicator is limited by the accuracy of the integrator.

### 2.3.3 A numerical example

As an example of the performance of the method, consider the parameterization of the two dimensional unstable manifold at  $p_0$ , computed to order  $N = 20$ . Figure 6 illustrates the effect of the choice of the eigenvector scaling on the decay rate of the Taylor coefficient. We remark that the magnitude of the last Taylor coefficient computed is a good heuristic indicator of the size of the truncation error. For example if we choose eigenvectors scaled to length one, we obtain the decay rate illustrated in the left frame of Figure 6, and we see that the norm of the largest coefficient of order twenty is about  $10^{-6}$ . On the other hand if we rescale to eigenvector to have length 1/2 then the coefficients decay as in the right frame of Figure 6, and the largest norm of any coefficient of order twenty is now about  $10^{-12}$ .

To visualize the parameterized local manifold we evaluate the polynomial approximation on the unit disk. First we take a Delaunay triangulation of the unit disk as illustrated in the left frame of Figure 7. This triangulation of the unit disk is pushed forward to the phase space  $\mathbb{R}^3$  by the polynomial parameterization, resulting in a triangulation of the two dimensional local unstable manifold as illustrated in the top left frame of Figure 8.

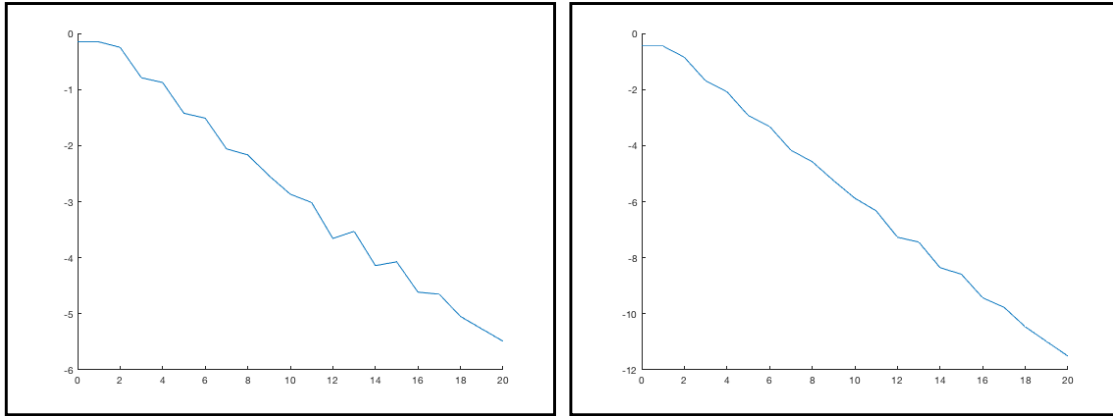


Figure 6: **Rescaling the eigenvector and coefficient decay:** the left frame shows the coefficient decay when the eigenvectors are scaled to unit length. The right frame is with scaling one half. Both figures plot coefficient magnitude  $\max_{i+j=n} \log(|p_{ij}|)$  (vertical axis) versus polynomial order  $n$  (horizontal axis). When the eigenvector is scaled to unit length we see that the order 20 coefficient are on the order of  $10^{-6}$ , which is small but far from machine epsilon. We should either increase the order of the polynomial or decrease the scale of the eigenvector. Indeed, when the scale is decreased to one half we see that the last coefficients have magnitude on the order of a few thousand multiples of machine epsilon.

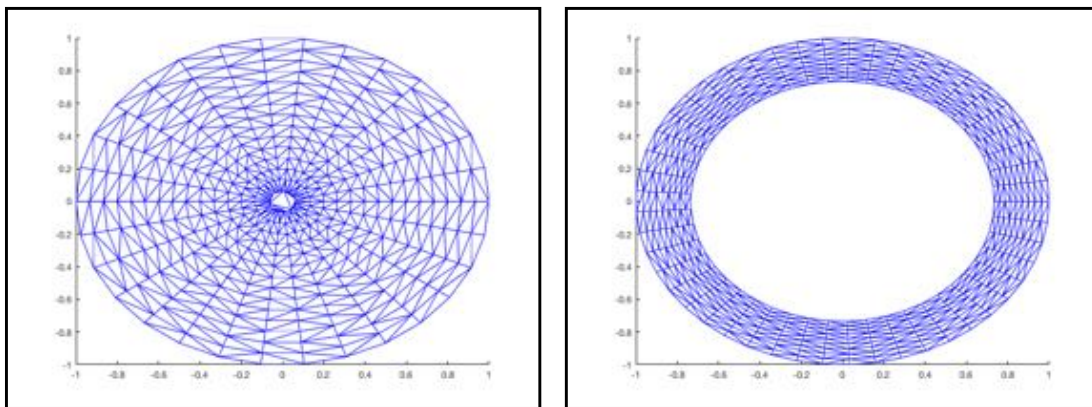


Figure 7: **Triangulating the local invariant manifold and fundamental domain:** for the local parameterization we subdivide the unit disk – fifteen radial subdivisions by 30 angular subdivisions (left). Since the domain is simply connected, the triangulation is computed using Delauney’s algorithm (built into MATLAB). For a fundamental domain we take the unit circle as the outer boundary, and the circle of radius  $|e^{-\lambda u \tau}|$  as the inner boundary of an annulus. We take ten radial subdivisions and fifty angular subdivisions. We compute a Delauney triangulation, but this “fills in the hole” of the annulus. This is fixed by removing triangles with a long side from the triangulation and results in the mesh illustrated in the right.

To “grow” a larger representation of the unstable manifold we choose a fundamental



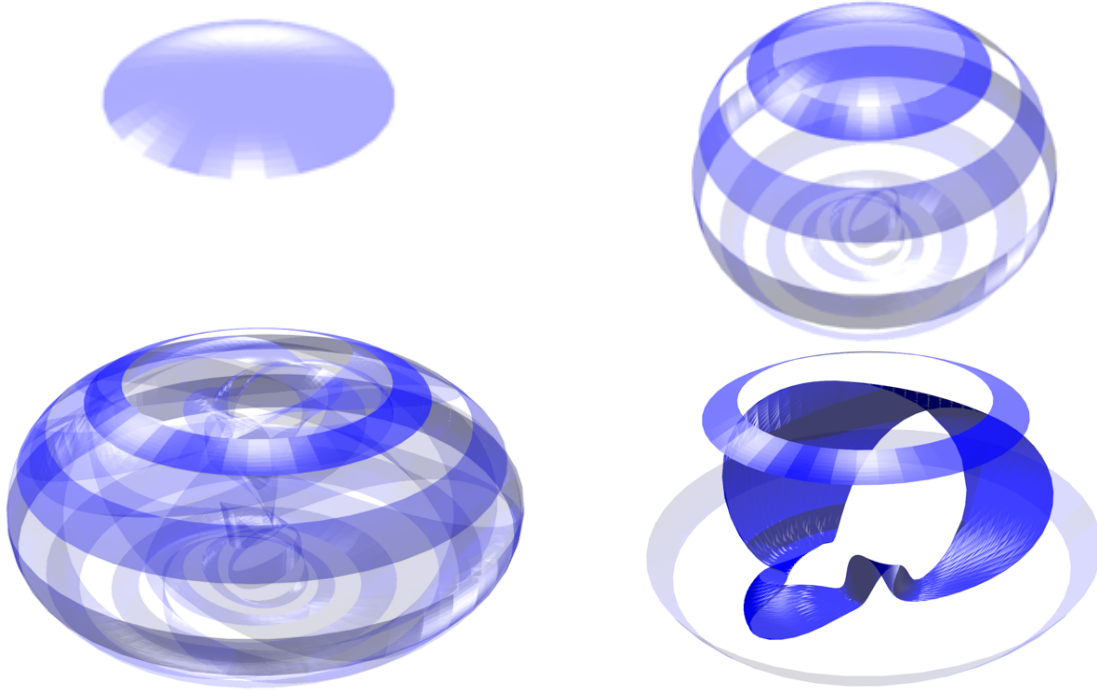


Figure 8: **Growing the unstable manifold one fundamental domain at a time:** (Top left) the initial local unstable manifold obtained using the parameterization method. (Top right) the initial local manifold parameterization as well as the first, third, fifth, seventh, ninth, eleventh, thirteenth, and fifteenth iterate of the fundamental domain. (Bottom left) the first through thirty third iterates of the fundamental domain. (Bottom right) the sixtieth iterate of the fundamental domain, and we see that the image is substantially folded. The first and sixth iterates are shown as well to provide the overall shape of the bubble. In the bottom frames the initial parameterized local unstable manifold is not shown.

domain, for example by taking  $\tau = 0.25$  and considering the annulus in parameter space formed by the boundary of the unit disk and by the circle of radius  $R = |e^{\lambda u \tau}| \approx 0.733$ . We mesh this annulus using 100 angular subdivisions and 40 radial subdivisions, as illustrated in the right frame of Figure 7. We lift this fundamental domain to the phase space and repeatedly apply the time  $\tau = 0.25$  map via numerical integration of the vertices of the triangulation. We refine the mesh whenever any side of a triangle in phase space gets too large. In the present work we measure “too large” just by looking at the resulting picture.

The top right, and bottom frames of Figure 8 illustrate the results of iterating a triangulation of a fundamental domain for the local unstable manifold at  $p_0$ , and we see that the “bubble” grows in a quite regular way. However, by the time we take 60 iterates the embedding of the initial annulus is becoming quite complicated and the results are difficult to parse. In this case it is much better to look at the union of many fundamental domains to try to understand the geometry of the bubble, as we do in the next section.

---

## 2.4 Accumulation of $W^u(p_0)$ on torus-like attractors

We now use the parameterization method/continuation scheme discussed in the previous sections to study the embedding of the unstable manifold of  $p_0$  for  $\alpha = 0, 0.6, 0.7, 0.8, 0.806, 0.9321, 0.95$  and  $1.1022$ . The results are illustrated in Figures 9 and 10.

We observe that at  $\alpha = 0$  the unstable manifold  $W^u(p_0)$  appears to accumulate on the attracting periodic orbit discussed in the introduction. When  $\alpha$  is larger, for example  $\alpha = 0.6, 0.7$ , and  $0.8$  the unstable manifold appears to accumulate on an attracting smooth invariant torus. For larger  $\alpha$  the pictures are a little harder to interpret. The unstable manifold still appears to accumulate on something like an attracting set (torus-like), but the set appears to be developing edges/folds. Then, for  $\alpha > 1$  the unstable manifold appears to accumulate on the  $z$ -axis.

These results suggest that the attracting periodic orbit undergoes a Neimark-Sacker bifurcation, giving rise to an invariant torus. In the next section we verify this by examining some Poincaré sections. Indeed the computations illustrated in Figures 9 and 10 suggest the  $x = 0, y > 0$  half plane as an appropriate choice of section. We first examine briefly the role of the stable manifold of  $p_1$ .

## 2.5 $W^s(p_1)$ as a separatrix

Recall that for  $\alpha < \alpha_* = 0.9321697517861$  the system has only one equilibrium point  $p_0$ , but that when  $\alpha > \alpha_*$  there are three equilibria, and the one we denote by  $p_1$  has a two dimensional stable manifold. A question of fundamental dynamical importance is: do  $W^s(p_1)$  and  $W^u(p_0)$  intersect transversally? Such intersections would give rise to heteroclinic connections from  $p_0$  to  $p_1$ .

Interestingly enough, it seems that for some interval of  $\alpha > \alpha_*$  there are no intersections at all. Instead, the stable manifold of  $p_1$  seems to form a separatrix which keeps the vortex bubble away from the stable attracting equilibrium solution  $p_2$ . So, for some range of  $\alpha > \alpha_*$  there are two basins of attraction, which appear to be separated by the stable manifold. The situation is illustrated in Figure 11.

When  $\alpha > \alpha_*$  is large enough, the unstable manifold of  $W^u(p_0)$  develops transverse intersections with  $W^s(p_1)$ . This global bifurcation gives rise to heteroclinic orbits from  $p_0$  to  $p_1$ . At the same time, the formation of intersections allows some orbits to cross from inside the bubble to the outside. That is, it becomes possible for an orbit starting in a neighborhood of the periodic orbit  $\gamma$  to get caught in the basin of attraction of  $p_2$ . Indeed once the manifolds intersect and  $W^s(p_1)$  ceases to be a separatrix, it appears that typical orbits are attracted to  $p_2$ . The situation is illustrated in Figures 12 and 13.

# 3 Poincaré sections and torus-like attractors

## 3.1 Bifurcations of Fixed Points of Poincaré Return Maps

To further investigate the dynamics we now examine a Poincaré section – again varying values of  $\alpha$ . Since our system is 3-dimensional, we take  $\Sigma$  a 2-dimensional surface transverse to the periodic orbit  $\gamma$ . Informed by the results of the unstable manifold calculations in

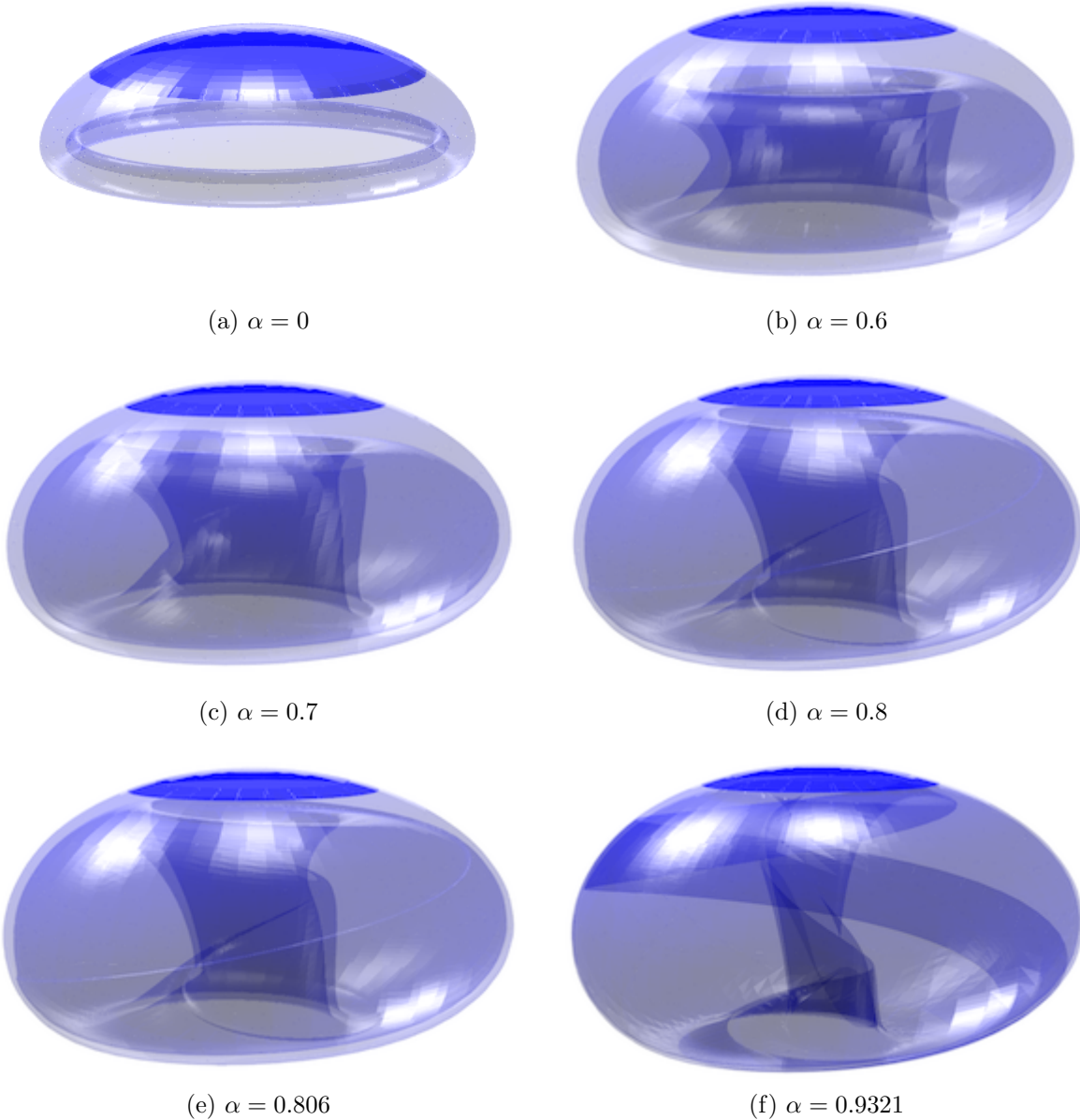


Figure 9: **Unstable manifold “bubble” for the saddle  $p_0$** : for the indicated values of  $\alpha$ . The computations suggest the existence of a periodic orbit which undergoes a Neimark-Sacker bifurcation. The phase space is then dominated by the resulting smooth invariant torus. The computations for higher  $\alpha$  suggest that the smoothness of the torus may breakdown as  $\alpha$  increases.

the previous section, we choose  $\Sigma$  to be the  $yz$  half plane with  $y > 0$ . Consider a point  $\hat{p}_0 = (y_0, z_0) \in \Sigma$  at time  $T = 0$ . As the trajectory starting at  $\hat{p}_0$  progresses it will return to  $\Sigma$  at  $\hat{p}_1$  after a certain period  $T(\hat{p}_0)$ . By considering all initial points on  $\Sigma$  we can define a

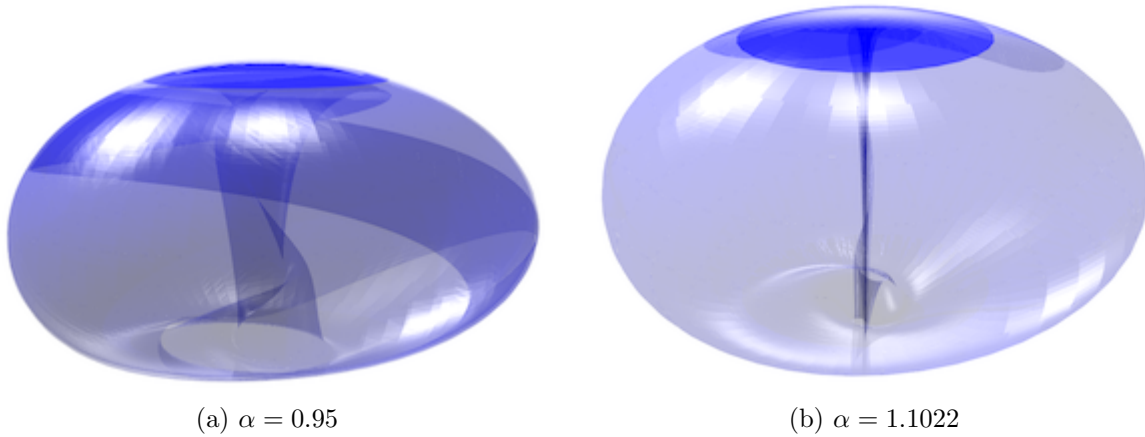


Figure 10: **High  $\alpha$  unstable manifold “bubbles” for  $p_0$** : Left:  $\alpha = 0.95$ . The bubble develops a “stripe” which is actually due to the manifold folding over itself as it accumulates on a torus like attractor. The folding suggests that the attractor itself has folds in its embedding. Right:  $\alpha = 1.1022$ . The unstable manifold now accumulates on the  $z$ -axis.

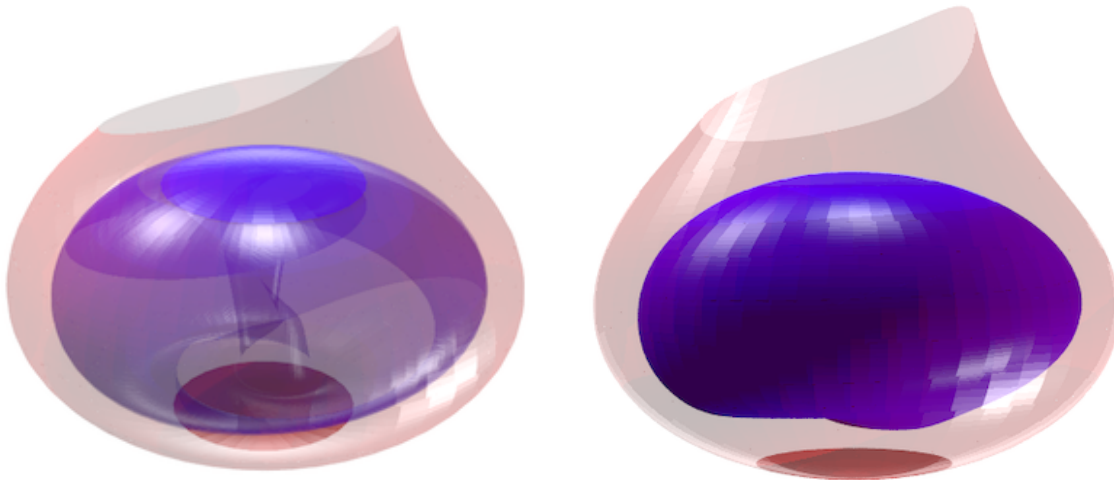


Figure 11: **2D stable and unstable manifolds of equilibria  $p_0$  and  $p_1$  for  $\alpha = 0.95$** . For this parameter value, we note that  $W^u(p_1)$  (blue) and  $W^s(p_2)$  (red) do not intersect at all, transversely or otherwise. We also remark that  $p_2$  (not shown) is just below  $p_1$  and is an attracting equilibrium point.

mapping  $P : \Sigma \rightarrow \Sigma$  such that  $P(\hat{p}_0) = \hat{p}_1$  and after  $k + 1$  intersections

$$\begin{aligned}
 P(\hat{p}_k) &= \hat{p}_{k+1} \\
 &= \phi(\hat{p}_k, T(\hat{p}_k)),
 \end{aligned}$$

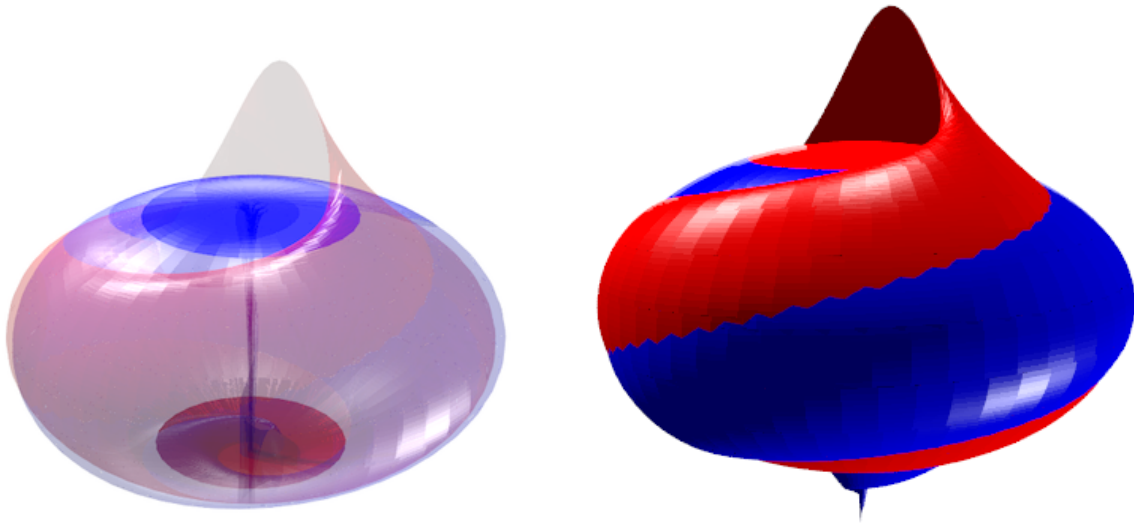


Figure 12: **2D stable and unstable manifolds of equilibria  $p_0$  and  $p_1$  for  $\alpha = 1.1022$ .** Here we see that  $W^u(p_1)$  (blue) and  $W^s(p_2)$  (red) appear to intersect transversely. The intersection curves are then heteroclinic orbits from  $p_0$  to  $p_1$ . The unstable manifold accumulates on the  $z$ -axis, as seen in the transparency on the left. The frame on the right suggests that the unstable manifold enters the basin of attraction of  $p_2$ . In fact, for  $\alpha = 1.1022$  it seems that  $p_2$  is the unique attractor.

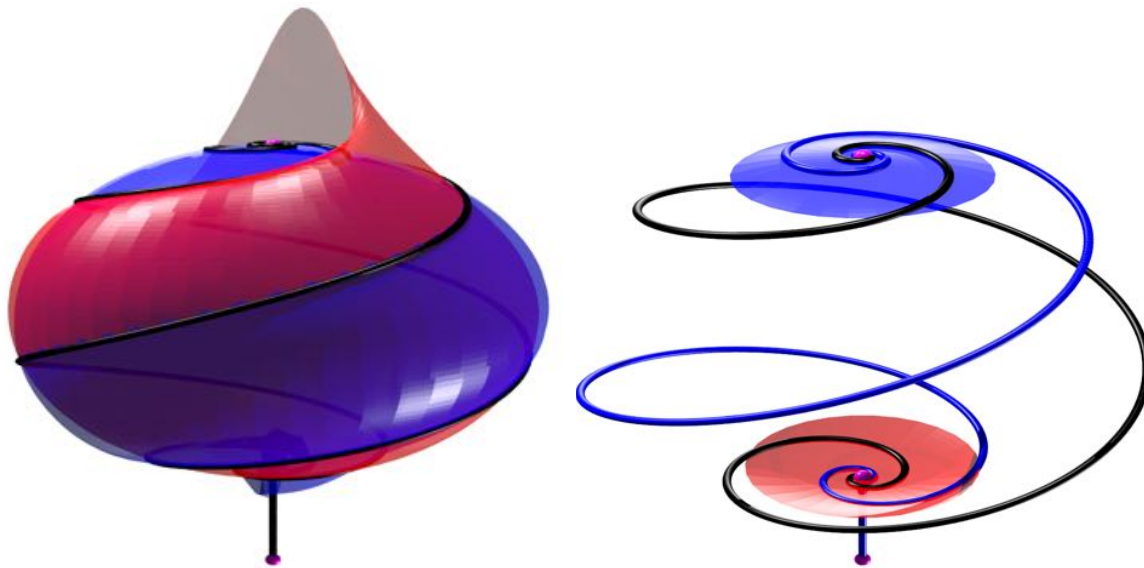


Figure 13: **Heteroclinic connections from  $p_0$  to  $p_1$  for  $\alpha = 1.1022$ .** Encouraged by the apparent transverse intersections seen in Figure 12, we locate heteroclinic orbit segments starting on  $W^u(p_0)$  and terminating on  $W^s(p_1)$  by applying a Newton scheme to the boundary value problem describing the segments. Observe that the heteroclinic orbit segments located are much smoother than the apparent intersection seen in Figure 12. The apparent irregularity of the intersection is due to the fact that we compute piecewise linear triangulations of the fundamental domain and its iterates.

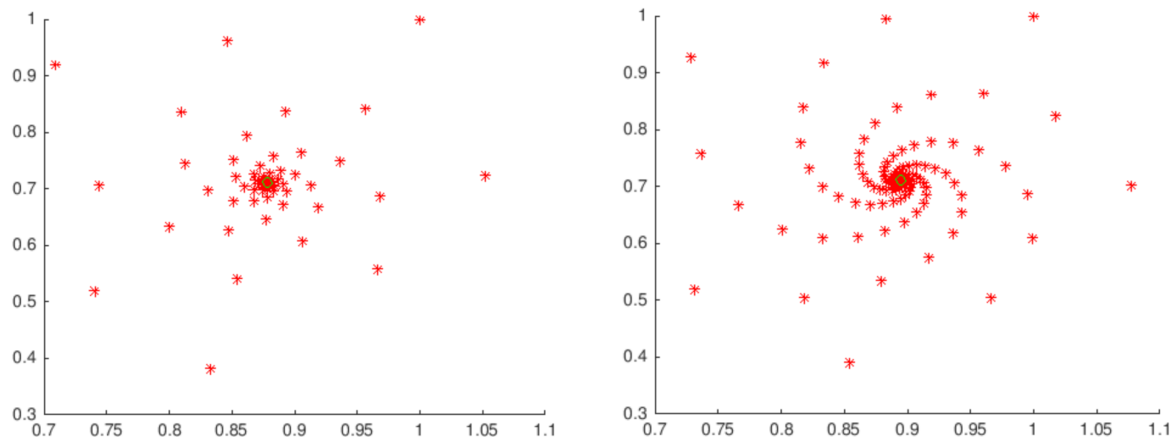


Figure 14: **Poincaré sections: attracting fixed point.** (Left) Attracting fixed point of the Poincaré return map when  $\alpha = 0.6$ . (Right) Attracting fixed point for the Poincaré return map when  $\alpha = 0.65$ .

where  $\Phi$  is the flow generated by Equation (1) and  $T(\hat{p}_k)$  is the return time. To find the return time  $T(\hat{p}_k)$ , we use the Newton Method

$$T(\hat{p}_{k+1}) = T(\hat{p}_k) - \frac{P(\hat{p}_k)}{P'(\hat{p}_k)},$$

where  $P'(\hat{p}_k) = f_1(\Phi(0, y_k, z_k, t(0, y_k, z_k)))$  and  $f_1(x, y, z) = (z - \beta)x - \delta y$ .

Computing the Poincaré return map for  $\alpha = 0$ , we found a periodic orbit at approximately  $(0.643155, 0.703726)$  on the  $yz$ -plane. For  $\alpha = 0.65$ , we still have an attracting fixed point for the Poincaré map but this time the trajectories converges faster. The attracting fixed point, as well as an orbit converging to it, are illustrated in Figure 14 for these two parameters.

For  $\alpha = 0.697144898322973$  the system undergoes a Neimark-Sacker bifurcation, a codimension one Hopf bifurcation for planar maps [50], where the attracting fixed point of  $P$  loses stability, and an invariant  $C^k$  torus is born ( $0 < k < \infty$ ). A case of codimension two has been studied in [6, 7, 8]. For  $\alpha = 0.7$  we have a repelling fixed point of the Poincaré return map at approximately  $(0.912262, 0.713478)$  and a stable limit cycle. For  $\alpha = 0.8$ , we have a repelling fixed of the Poincaré return map at approximately  $(0.943218, 0.713691)$ . The dynamics in the section just at and just after the bifurcation are illustrated in Figure 15. The dynamics on the invariant circle appear to be conjugate to a rotation, though the orderly dynamics break up for larger  $\alpha$  as described in the next section.

### 3.2 Torus-Chaos

We will now investigate possible routes to chaos for our system, but first we review some standard material on invariant tori of dissipative systems. An excellent reference for this material is [24]. So, consider an  $N$ -dimensional dynamical system with  $N \geq 3$  and  $\dot{x} = f(x, \mu)$ , where components of  $f$  are  $C^r$ ,  $r \geq 3$ , and  $\mu$  is the system parameter. Suppose that at  $\mu = \mu_0$  a smooth attracting torus  $T^2(\mu_0)$  is born in some region of our system and

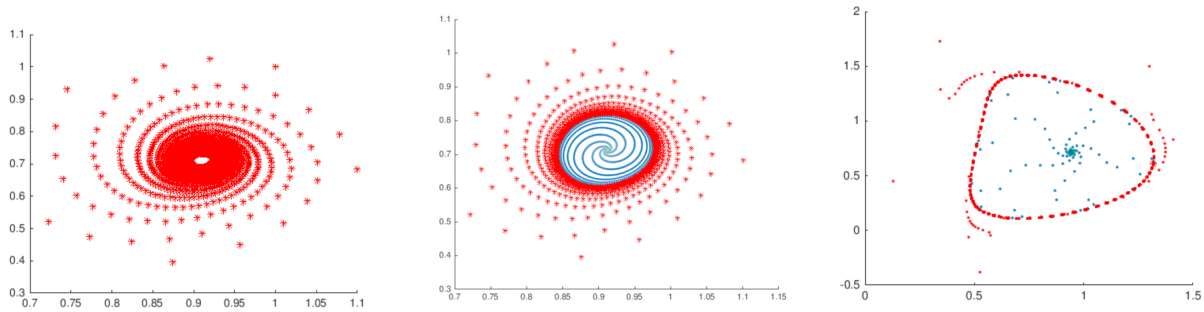


Figure 15: **Poincaré sections: attracting fixed point.** (Left) Neimark-Sacker bifurcation for  $\alpha \approx 0.697144$ , (Center) Repelling fixed point of the Poincaré map and  $\omega$ -limit cycle for  $\alpha = 0.7$ , (Right) Repelling fixed point of the Poincaré map and  $\omega$ -limit cycle for  $\alpha = 0.8$ . In the center and right frames blue represents orbit points diverging from the repelling fixed point and converging to the attracting invariant circle from inside. In all frames red represents orbit points converging to the attracting invariant circle from outside. This circle itself is located by iterating the Poincaré map sufficiently long.

has a robust structure of stable and saddle cycles. That is, suppose that the surface of the resonance torus is formed by the closure of the unstable manifold  $W^s$  of a saddle cycle accumulating to a stable cycle. We then have a resonance region in the sense of [24]. The situation is illustrated in Figure 16.

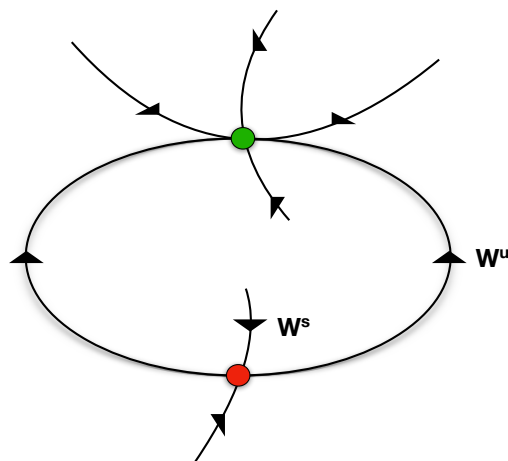


Figure 16: Schematic of the Poincaré section of a resonance torus  $T^2$ , green dots are stable cycles while red dots are saddle cycles.

Now suppose that the invariant torus does not exist at some later parameter  $\mu = \mu_1$ . Then for the continuous curve  $\mu(s)$ , where  $s \in [0, 1]$ ,  $\mu(0) = \mu_0$ ,  $\mu(1) = \mu_1$ , there exists a value  $s = s^*$  such that at  $\mu(s^*)$ , the torus  $T^2$  is destroyed and no longer exists in our system for at least some arbitrary value of  $s$ , close to  $s^*$ ,  $s > s^*$  [24]. Assume that for all  $0 \leq s < s^*$  the attracting set of our system coincides with the torus  $T^2(\mu(s))$ . Furthermore

suppose that in the limit  $s \rightarrow s^*$ , the unstable manifold  $W^u(\mu(s))$  of the saddle cycle does not enclose periodic orbits, different from the stable and saddle cycles. Under these assumptions, the *theorem on two-dimensional torus breakdown* [24] asserts the following three possible mechanisms of  $T^2$  destruction: (i) due to the loss of cycle stability; (ii) as a consequence of the emergence of a homoclinic tangency between  $W^u$  and  $W^s$  of the saddle cycle, and (iii) due to a tangent bifurcation of the stable and saddle cycles on  $T^2$ . Before being destroyed,  $T^2$  loses its smoothness for  $s > s^{**}$ , i.e.,  $T^2(\mu(s^{**} < s < s^*))$  is *homeomorphic* but not *diffeomorphic* to the torus.

For  $\alpha = 0.81$ , there are two period three cycles of the Poincaré map, one stable and the other one a saddle. By stable and saddle cycle we mean that there exists  $k \in \mathbb{N}$ ,  $k < \infty$ , such that  $P^k(p) = p$ , with  $p, P^i(p) \in \Sigma$ ,  $1 \leq i \leq k$ . Therefore one cycle corresponds to  $k$  iterates of  $p$  in  $\Sigma$ ; we denote  $k$  to be the period of our cycle and check its stability by computing the eigenvalues of  $p$ .

To visualize the appearance of the resonance torus we compute the one dimensional unstable manifolds  $W^u$  of the saddle cycle in the Poincaré section. We look for a parameter value of  $\alpha$  so that a topological circle containing the two cycles of period three is formed. Let  $p_u$  denote the saddle cycle and  $\lambda_u$  denote the unstable eigenvalue of  $DP^3(p_u) = D(P(P(P(p_u))))$  (using finite difference method). Let  $\xi_u$  denote the associated choice of eigenvector for our saddle cycle. We first rescale our eigenvectors to length  $10^{-5}$ , then compute the linearization of the unstable manifold for  $p_u$  with  $h(s) = p_u + s\xi_u$  where  $s \in \{k \mid 1 \leq |k| \leq \lambda_u\}$ . Finally, we compute  $\phi(P(h(s)), T)$  for a fixed time  $T$  and obtain the unstable manifold of  $p_u$  on  $\Sigma$ . We can repeat the same process with the appropriate eigenvalues and eigenvectors and consider the vector field  $-f$  from Equation (1) for the case of the stable manifold of  $p_u$ .

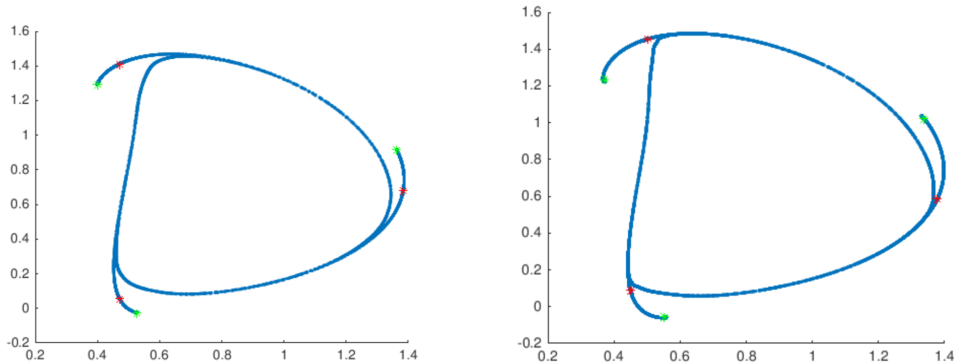


Figure 17: **Unstable manifold of the saddle period three cycle in the Poincaré section.** The three red dots illustrate the saddle cycle while the three green points illustrate the attracting cycle. The blue points are on the unstable manifold of the saddle cycle. In both cases one side of the unstable manifold accumulates on the attracting invariant circle, while the other side accumulates on the attracting period three cycle. In the left frame ( $\alpha = 0.82$ ) the saddle is far from the invariant circle but in the right frame ( $\alpha = 0.8224$ ) it has moved much closer.

We report that the  $C^0$  resonance torus is born somewhere between  $\alpha = 0.82$  and  $\alpha = 0.825$ . Upon further numerical analysis, we note that this bifurcation (from  $C^k$  torus,  $0 <$



$k < \infty$ , to  $C^0$  torus) happens in the following manner: we first have that one side of  $W^u$  of the saddle cycle converges to the attracting orbit while the other side wraps around the attracting limit cycle originating from the Neimark-Sacker bifurcation. We then have heteroclinic saddle connections on  $\Sigma$  which leads to transverse intersections of  $W^u$  and  $W^s$  of the saddle cycle. This transverse intersection gives rise to the presence of Smale horseshoes and thus chaotic dynamics. We also remark that before and after those transverse intersections we have tangencies of  $W^s$  and  $W^u$  of the saddle cycle, one on each side of  $W^s$  of the saddle cycle. Finally,  $W^u$  of the saddle cycle detaches completely from  $W^s$  and gets caught in an attracting region of the stable cycle.

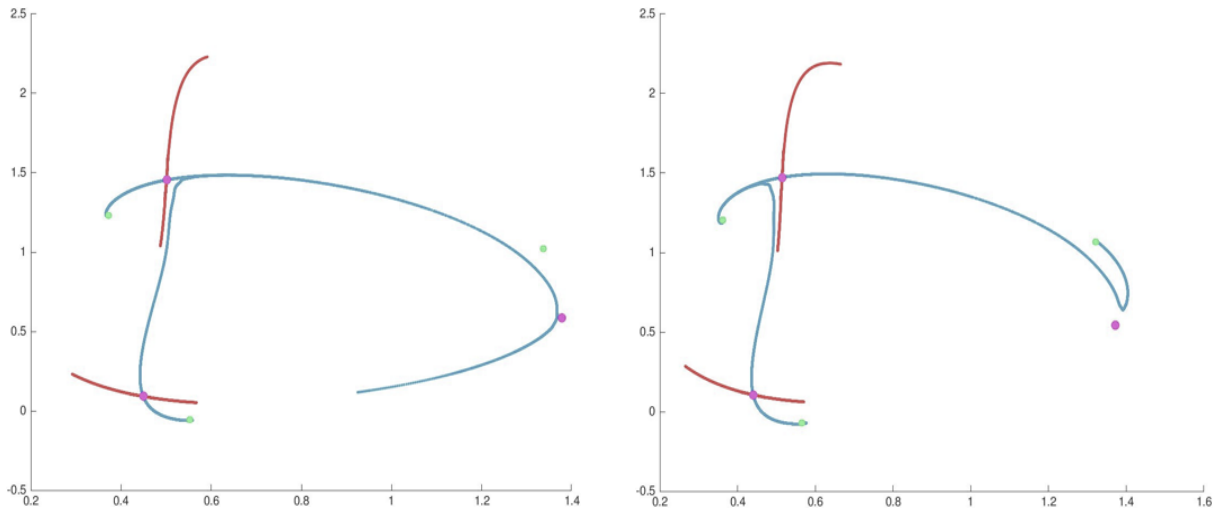


Figure 18: Stable manifold of the saddle cycle  $W^s$  is red and unstable manifold of the saddle cycle  $W^s$  is blue. The stable cycle on the Poincaré section is red and the saddle cycle is magenta. (Left) at  $\alpha = 0.822$  one side of  $W^u$  of the saddle cycle goes to the attracting orbit while the other side wraps around the attracting invariant circle. (Right) at  $\alpha = 0.826$   $W^u$  of the saddle cycle detaches completely from  $W^s$  of the same saddle cycle and gets caught in an attracting region of the stable cycle.

After this bifurcation we later note that for  $\alpha \geq 0.9$ , the spirals going to the stable period three cycle of the Poincaré section start to have some waves due to complex conjugate eigenvalues. We also note that for  $0.92 < \alpha < 0.93$ ,  $W^u$  of the saddle cycle is distorted and another tangency of  $W^u$  and  $W^s$  of the saddle cycle occurs. Beyond this value for which this tangency happens, we again have transverse intersections of  $W^u$  and  $W^s$  of the saddle cycle and chaotic dynamics ensues for the second time. From this point, our  $T^2$  no longer exists. For  $\alpha = 0.95$ , the spiraling waves are no longer present going into the stable cycle, the torus  $T^2$  in phase space is destroyed and trajectories fall in a set with fractal dimension  $2 + d$ ,  $d < 1$ . Both period three cycles have moved inside the invariant set.

In summary after the Neimark-Sacker bifurcation, numerical analysis suggests that for our bifurcation parameter  $\alpha$ , the system enters into a chaotic state twice, once from the torus bifurcation from  $C^k$  to  $C^0$ , and another one from the destruction of the  $C^0$  torus. We note that for both torus bifurcations we have a tangency of the unstable and the stable manifolds of the saddle cycle which then leads to transverse intersections of  $W^u$  and  $W^s$  of the saddle

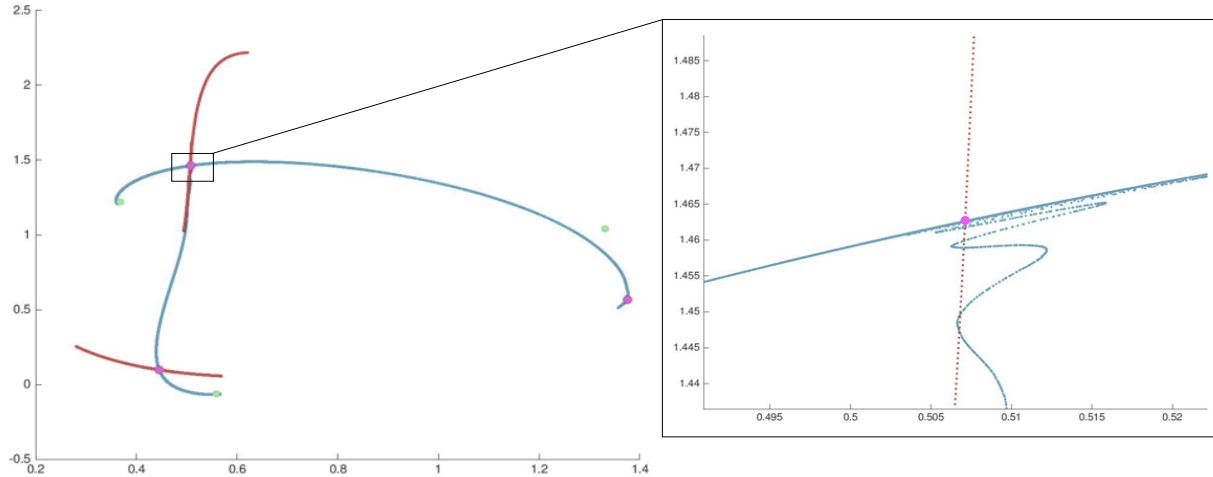


Figure 19: Colors have the same meaning as in Figure 18. At  $\alpha = 0.8225$  We have transverse intersections of  $W^u$  and  $W^s$  of the saddle cycle which leads to the presence of Smale horseshoes and thus chaotic dynamics.

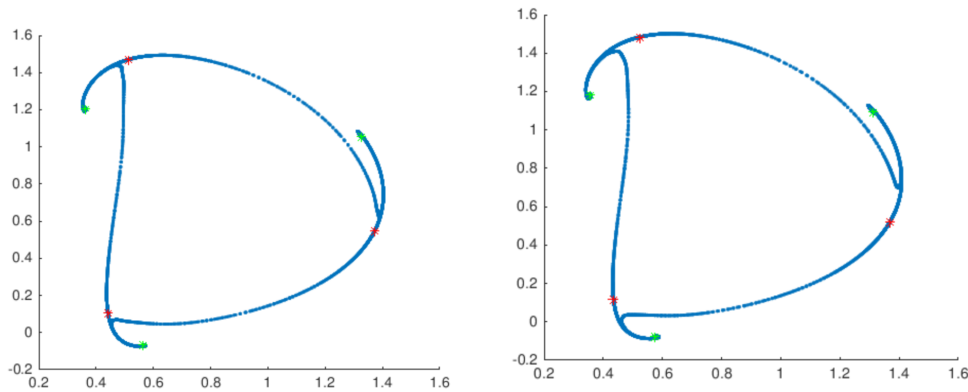


Figure 20: **Unstable manifold of the saddle period three orbit in the Poincaré section.** Colors have the same meaning as in Figure 17. (Left) At  $\alpha = 0.825$  the saddle period three cycle has collided with the invariant circle, and both period three cycles and the unstable manifold are inside the invariant set: the resonance torus is born. (Right) At  $\alpha = 0.83$  the spiral at the attracting fixed point is more pronounced. Since the invariant circle contains a saddle focus (in fact three) the circle is not smooth.

cycle and thus chaotic dynamics. Moreover, having obtained such information through the examination of Poincaré sections, we can integrate the invariant structures in phase space to gain an even better understanding of the dynamics. See for example the “cut-aways” of the invariant tori in Figures 26, 27 and 28.

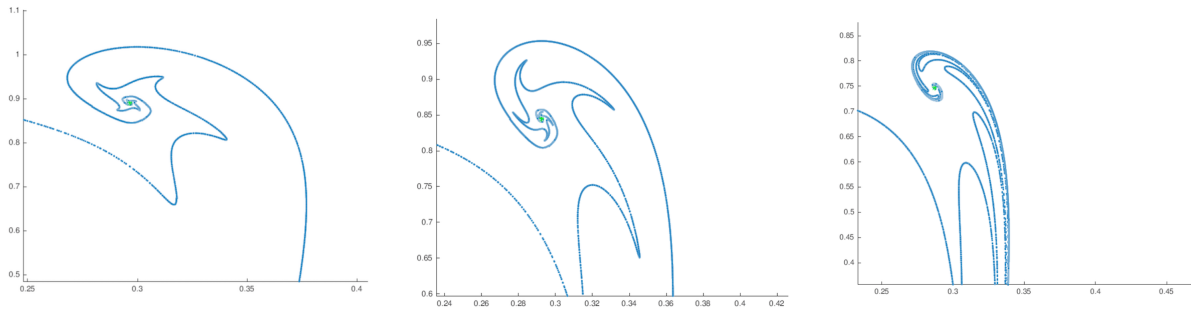


Figure 21: **Unstable manifold of the saddle period three orbit in the Poincaré section.** Colors have the same meaning as in Figure 17. Closeups on the attracting periodic point for different values of  $\alpha$  and it is clear that the invariant circle is becoming increasingly irregular.

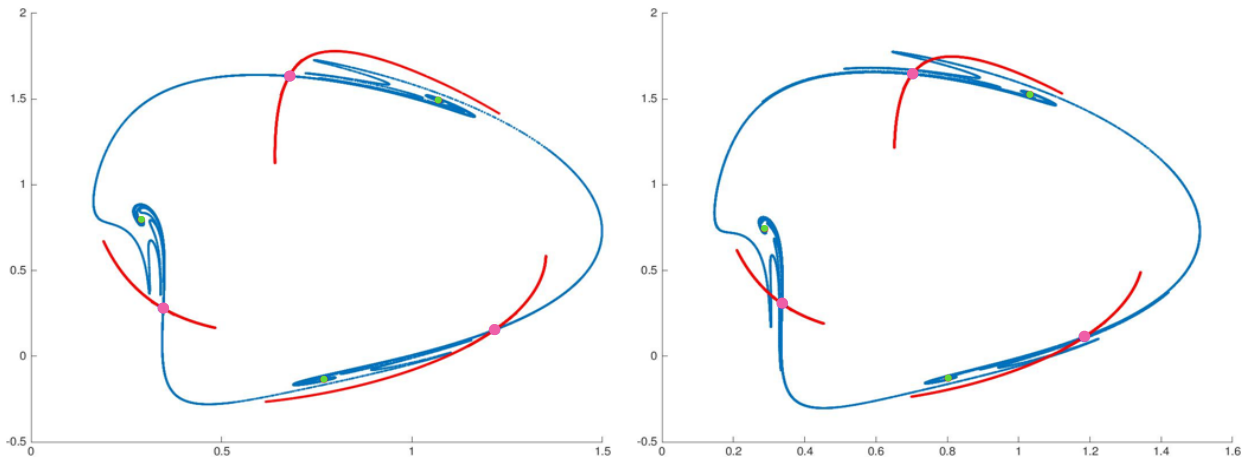


Figure 22: Stable manifold of the saddle cycle  $W^s$  is red and unstable manifold of the saddle cycle  $W^u$  is blue. The stable cycle on the Poincaré section is green and the saddle cycle is magenta. (Left) For  $\alpha = 0.92$ , we have that the unstable manifold  $W^u$  of the saddle cycle is within a small neighborhood of the stable manifold  $W^s$  of the saddle cycle. (Right) For  $\alpha = 0.93$ , we have transverse intersections of the stable and unstable manifolds of the saddle cycle (magenta) which give rise to a Smale Horseshoe and thus chaotic dynamics.

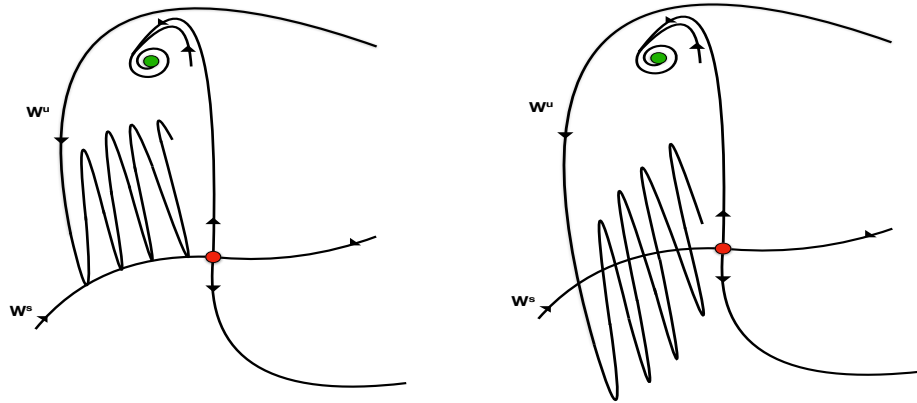


Figure 23: **Schematic of the tangency.** (Left) For some parameter value  $0.92 < \alpha < 0.93$ , a tangency of  $W^u$  and  $W^s$  of the saddle cycle occurs. (Right) Intersections of stable and unstable separatrices of a saddle cycle (red) which give rise to a Smale Horseshoe.

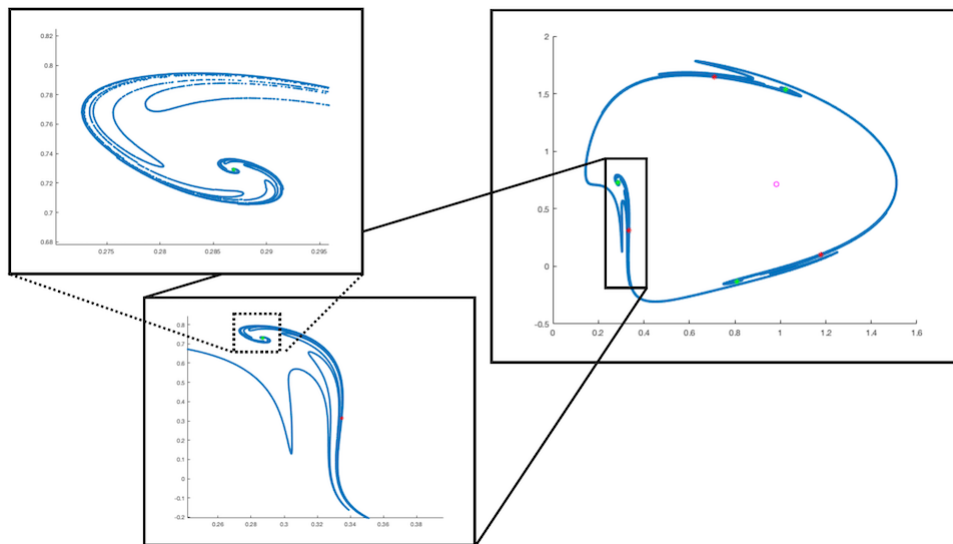


Figure 24: Spiraling waves going into the stable cycle at  $\alpha = 0.9321$ . Numerical analysis reveals that for this parameter value, the stable and unstable manifold of the saddle cycle intersect, giving rise to chaotic dynamics.

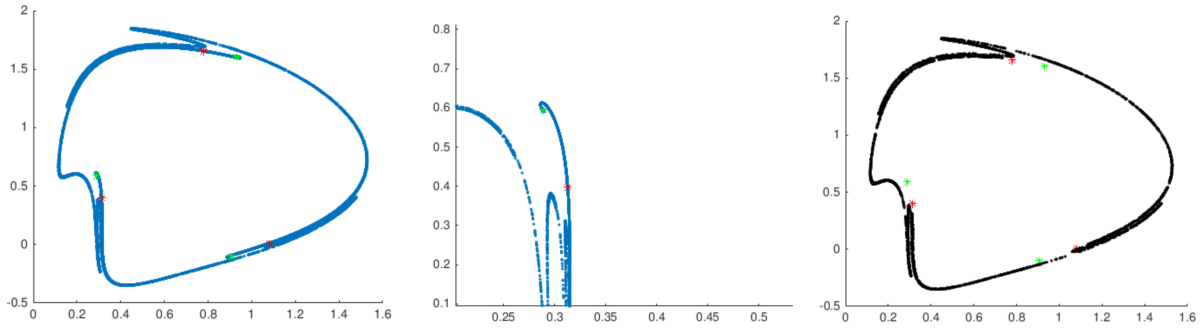


Figure 25: All three figures were plotted using  $\alpha = 0.95$ . Left) Unstable manifold of the saddle period three cycle in the Poincaré section, colors have the same meaning as in Figure 17. (Center) The spiraling waves are no longer present going into the stable cycle. (Right) The torus  $T^2$  in phase space is destroyed and trajectories fall in a set with fractal dimension  $2 + d$ ,  $d < 1$ . Both period three cycles have moved inside the invariant set (black).

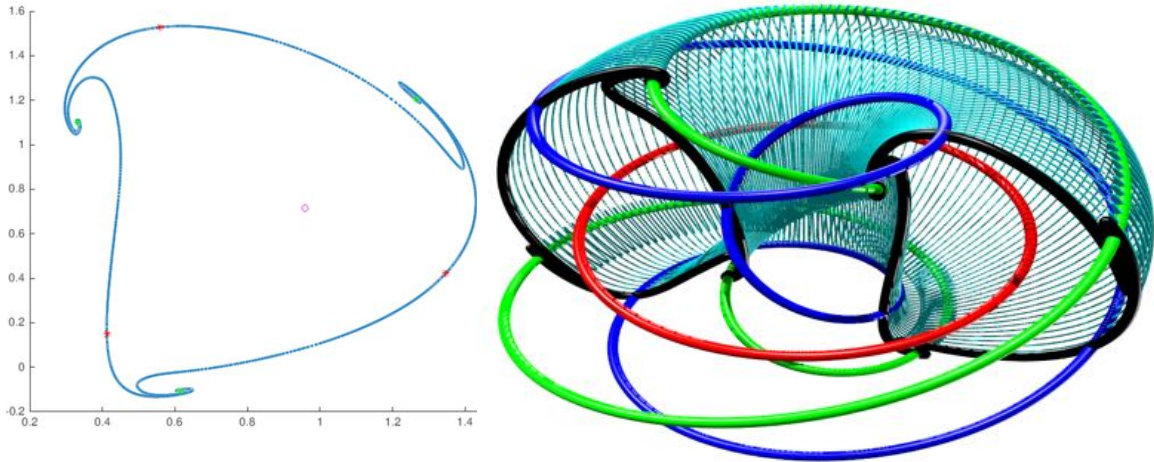


Figure 26: **Cut-away at  $\alpha = 0.85$ :** The left frame recalls the invariant set in the Poincaré section when  $\alpha = 0.85$ , which is a resonance torus formed by two period three cycles. The right frame illustrates the corresponding invariant set in phase space. The red curve is the repelling periodic orbit which originally underwent the Neimark-Sacker bifurcation. The green curve is the attracting periodic orbit corresponding to the attracting period three cycle, while the blue curve is the saddle periodic orbit corresponding to the period three saddle cycle in the Poincaré section. The half torus colored in teal rings is obtained by integrating the invariant set from the Poincaré section for half the period of the unstable orbit. The resulting invariant set is a topological, but not smooth, invariant resonance torus.

## 4 Conclusions and Discussion

We studied the dynamics of the Langford system given by the vector field in Equation (1), which is an example of a rotating collapsing fluid. We looked first at the phase portraits of the system for different parameter values of  $\alpha$  while keeping the other parameters fixed. We plotted 2D unstable manifolds for the corresponding saddle equilibrium points and noted

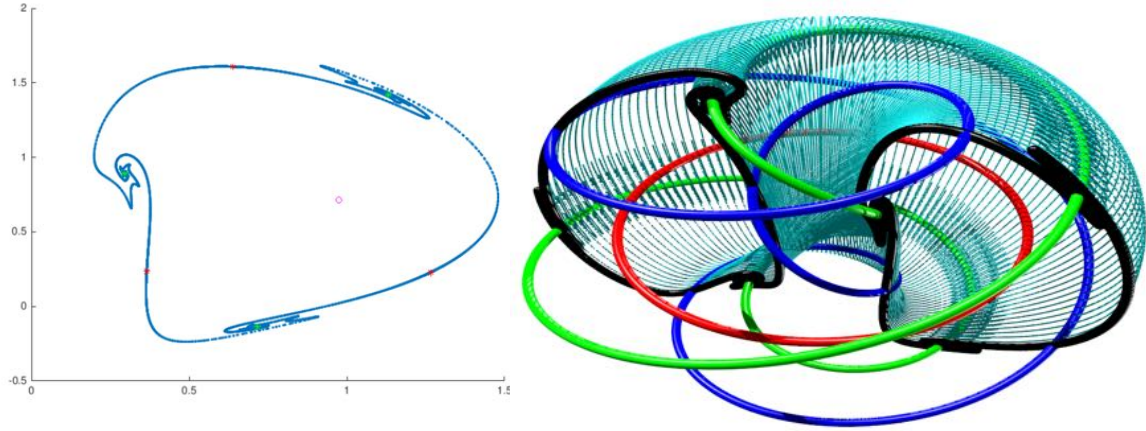


Figure 27: **Cut-away at  $\alpha = 0.9$ :** same color scheme as in Figure 26. Now the spirals into the attracting periodic orbit develop the spiralling waves and the torus is less regular.

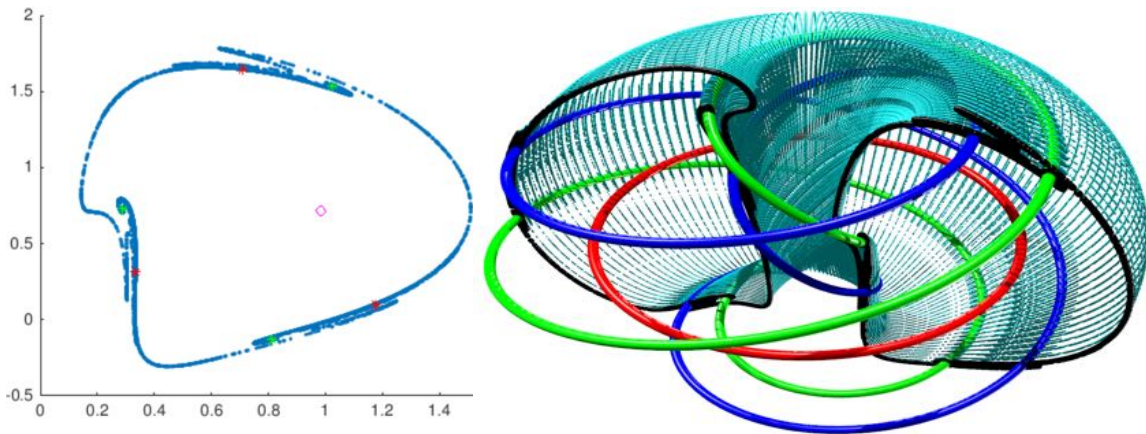


Figure 28: **Cut-away at  $\alpha = 0.929$ :** same color scheme as in Figure 26. The figure illustrates the dynamics in phase space before the development of torus-chaos.

that there was a ring inside the manifold which later reveals itself to be an attracting periodic orbit when  $\alpha = 0$  and  $0.6$ . For  $\alpha = 0.806$  and  $\alpha = 0.9321$ , by looking at the 2D unstable manifolds, we noticed a thick dark line on the surface of the bubble which we later found to be a pair of attracting and saddle periodic orbits. For  $\alpha > 0.9321697517861$ , the second and third equilibrium points of the system have purely real parts and no imaginary parts. For  $\alpha = 0.95$ , the  $\alpha$  parameter value for the popular chaotic attractor, the 2D stable manifold acts as separatrix and seems to hold the attractor together; and for  $\alpha = 1.1022$ , we noted that all trajectories go to the attracting equilibrium due to transverse connecting orbits.

By computing the Poincaré return maps for  $\alpha$  between  $0$  and  $0.65$ , we found attracting fixed-points. For  $\alpha = 0.697144898322973$ , the system undergoes a *Neimark-Sacker bifurcation* and an invariant  $C^k$  torus ( $0 < k < \infty$ ) is born beyond this point. For  $\alpha = 0.7$ , we have a repelling fixed point of the Poincaré return map and a stable limit cycle. We then investigated possible routes to chaos for the system. For  $\alpha = 0.81$ , two period three cycles of the Poincaré map are found, one stable and the other one a saddle. We then computed

---

one dimensional unstable manifolds ( $W^s$ ) of the saddle cycle on the Poincaré section. The numerical evidence suggests that a resonance torus appears somewhere between  $\alpha = 0.82$  and  $\alpha = 0.825$  and is caused by the destruction of a  $C^k$  torus resulting from transverse intersections of the stable and unstable manifolds of a saddle cycle on the Poincaré section. Also, for  $0.92 < \alpha < 0.93$ ,  $W^u$  of the saddle cycle which forms the torus surface is distorted and a tangency of  $W^u$  and  $W^s$  of the saddle cycle occurs. At this moment ( $\alpha = \alpha^*$ ) a structurally unstable homoclinic trajectory arises and  $T^2$  does not exist above that  $\alpha$  parameter value for which this tangency occurs. For  $\alpha > \alpha^*$ , robust homoclinic structures of the cycles and of chaotic trajectories are formed in their vicinity. However, the stable cycle is still stable and remains as an attractor. We conclude that the system enters into a chaotic state twice for our bifurcation parameter, one for each torus bifurcation.

Finally, we mention that the present work serves also as a prequel to a work in progress where we will give computer assisted proofs of many of the numerical conjectures presented here. These proofs are based on the techniques developed in [45, 48, 51] for validating bounds on local manifold parameterizations and computer assisted proofs for heteroclinic connections, the methods developed in [52, 53, 54, 55] for rigorous integration of vector fields and computer assisted proof in Poincaré sections, and the methods of [56, 57] for obtaining validated error bounds on stable/unstable manifolds in Poincaré sections.

## 5 Acknowledgments

The authors would like to thank Jordi-Lluís Figueras, Maciej Capiński, and Vincent Naudot for many helpful suggestions and invaluable insights. We owe also a special thanks to Takahito Mitsui for bringing the paper of Langford [10] to our attention after reading an earlier version of this manuscript.

## References

- [1] Ju. I. Neĭmark. Some cases of the dependence of periodic motions on parameters. *Dokl. Akad. Nauk SSSR*, 129:736–739, 1959.
- [2] Robert John Sacker. *ON INVARIANT SURFACES AND BIFURCATION OF PERIODIC SOLUTIONS OF ORDINARY DIFFERENTIAL EQUATIONS*. ProQuest LLC, Ann Arbor, MI, 1964. Thesis (Ph.D.)–New York University.
- [3] Seung-hwan Kim, R. S. MacKay, and J. Guckenheimer. Resonance regions for families of torus maps. *Nonlinearity*, 2(3):391–404, 1989.
- [4] C. Baesens, J. Guckenheimer, S. Kim, and R. S. MacKay. Three coupled oscillators: mode-locking, global bifurcations and toroidal chaos. *Phys. D*, 49(3):387–475, 1991.
- [5] Kuniyiko Kaneko. Transition from torus to chaos accompanied by frequency lockings with symmetry breaking. In connection with the coupled-logistic map. *Progr. Theoret. Phys.*, 69(5):1427–1442, 1983.

- 
- [6] Alain Chenciner. Bifurcations de points fixes elliptiques. I. Courbes invariantes. *Inst. Hautes Études Sci. Publ. Math.*, (61):67–127, 1985.
- [7] A. Chenciner. Bifurcations de points fixes elliptiques. II. Orbites périodiques et ensembles de Cantor invariants. *Invent. Math.*, 80(1):81–106, 1985.
- [8] Alain Chenciner. Bifurcations de points fixes elliptiques. III. Orbites périodiques de “petites” périodes et élimination résonnante des couples de courbes invariantes. *Inst. Hautes Études Sci. Publ. Math.*, (66):5–91, 1988.
- [9] R. S. MacKay. Transport in 3D volume-preserving flows. *J. Nonlinear Sci.*, 4(4):329–354, 1994.
- [10] W. F. Langford. Numerical studies of torus bifurcations. In *Numerical methods for bifurcation problems (Dortmund, 1983)*, volume 70 of *Internat. Schriftenreihe Numer. Math.*, pages 285–295. Birkhäuser, Basel, 1984.
- [11] Marta Canadell and Àlex Haro. Computation of quasi-periodic normally hyperbolic invariant tori: algorithms, numerical explorations and mechanisms of breakdown. *J. Nonlinear Sci.*, 27(6):1829–1868, 2017.
- [12] Marta Canadell and Àlex Haro. Computation of quasiperiodic normally hyperbolic invariant tori: rigorous results. *J. Nonlinear Sci.*, 27(6):1869–1904, 2017.
- [13] X. Cabré, E. Fontich, and R. de la Llave. The parameterization method for invariant manifolds. I. Manifolds associated to non-resonant subspaces. *Indiana Univ. Math. J.*, 52(2):283–328, 2003.
- [14] X. Cabré, E. Fontich, and R. de la Llave. The parameterization method for invariant manifolds. II. Regularity with respect to parameters. *Indiana Univ. Math. J.*, 52(2):329–360, 2003.
- [15] X. Cabré, E. Fontich, and R. de la Llave. The parameterization method for invariant manifolds. III. Overview and applications. *J. Differential Equations*, 218(2):444–515, 2005.
- [16] Z.B. Stone and H.A. Stone. Imaging and quantifying mixing in a model droplet micromixer. *Phys. Fluids*, 17:063103, 2005. <https://doi.org/10.1063/1.1929547>.
- [17] K. E. Lenz, H. E. Lomelí, and J. D. Meiss. Quadratic volume preserving maps: an extension of a result of Moser. *Regul. Chaotic Dyn.*, 3(3):122–131, 1998. J. Moser at 70 (Russian).
- [18] H. R. Dullin and J. D. Meiss. Quadratic volume-preserving maps: invariant circles and bifurcations. *SIAM J. Appl. Dyn. Syst.*, 8(1):76–128, 2009.
- [19] Shawn C. Shadden, John O. Dabiri, and Jerrold E. Marsden. Lagrangian analysis of fluid transport in empirical vortex ring flows. *Phys. Fluids*, 18(4):047105, 11, 2006.



- 
- [20] Takashi Matsumoto, Leon O. Chua, and Ryuji Tokunaga. Chaos via torus breakdown. *IEEE Trans. Circuits and Systems*, 34(3):240–253, 1987.
- [21] O. Sosnovtseva and E. Mosekilde. Torus destruction and chaos-chaos intermittency in a commodity distribution chain. *Internat. J. Bifur. Chaos Appl. Sci. Engrg.*, 7(6):1225–1242, 1997.
- [22] Taoufik Bakri, Yuri A. Kuznetsov, and Ferdinand Verhulst. Torus bifurcations in a mechanical system. *J. Dynam. Differential Equations*, 27(3-4):371–403, 2015.
- [23] Taoufik Bakri and Ferdinand Verhulst. Bifurcations of quasi-periodic dynamics: torus breakdown. *Z. Angew. Math. Phys.*, 65(6):1053–1076, 2014.
- [24] Vadim S. Anishchenko, Vladimir Astakhov, Alexander Neiman, Tatjana Vadivasova, and Lutz Schimansky-Geier. *Nonlinear dynamics of chaotic and stochastic systems*. Springer Series in Synergetics. Springer, Berlin, second edition, 2007. Tutorial and modern developments.
- [25] Arash Mohammadi. The Aizawa Attractor. <https://www.youtube.com/watch?v=RBqbQUu-p00>, November 2017.
- [26] Michael Gagliardo. 3d printing chaos. In Carlo Séquin Eve Torrence, Bruce Torrence and Kristóf Fenyvesi, editors, *Proceedings of Bridges 2018: Mathematics, Art, Music, Architecture, Education, Culture*, pages 491–494, Phoenix, Arizona, 2018. Tesselations Publishing. Available online at <http://archive.bridgesmathart.org/2018/bridges2018-491.pdf>.
- [27] <http://chaoticatmospheres.com/mathrules-strange-attractors>. “Strange Attractors.” Chaotic Atmospheres.
- [28] A. Haro and R. de la Llave. A parameterization method for the computation of invariant tori and their whiskers in quasi-periodic maps: rigorous results. *J. Differential Equations*, 228(2):530–579, 2006.
- [29] À. Haro and R. de la Llave. A parameterization method for the computation of invariant tori and their whiskers in quasi-periodic maps: numerical algorithms. *Discrete Contin. Dyn. Syst. Ser. B*, 6(6):1261–1300 (electronic), 2006.
- [30] A. Haro and R. de la Llave. A parameterization method for the computation of invariant tori and their whiskers in quasi-periodic maps: explorations and mechanisms for the breakdown of hyperbolicity. *SIAM J. Appl. Dyn. Syst.*, 6(1):142–207 (electronic), 2007.
- [31] Gemma Huguet and Rafael de la Llave. Computation of limit cycles and their isochrons: fast algorithms and their convergence. *SIAM J. Appl. Dyn. Syst.*, 12(4):1763–1802, 2013.
- [32] Antoni Guillamon and Gemma Huguet. A computational and geometric approach to phase resetting curves and surfaces. *SIAM J. Appl. Dyn. Syst.*, 8(3):1005–1042, 2009.

- 
- [33] Marta Canadell and Àlex Haro. Parameterization method for computing quasi-periodic reducible normally hyperbolic invariant tori. In *Advances in differential equations and applications*, volume 4 of *SEMA SIMAI Springer Ser.*, pages 85–94. Springer, Cham, 2014.
- [34] J. D. Mireles James and Maxime Murray. Chebyshev-Taylor parameterization of stable/unstable manifolds for periodic orbits: implementation and applications. *Internat. J. Bifur. Chaos Appl. Sci. Engrg.*, 27(14):1730050, 32, 2017.
- [35] Maxime Breden, Jean-Philippe Lessard, and Jason D. Mireles James. Computation of maximal local (un)stable manifold patches by the parameterization method. *Indag. Math. (N.S.)*, 27(1):340–367, 2016.
- [36] Jan Bouwe van den Berg, Jason D. Mireles James, and Christian Reinhardt. Computing (un)stable manifolds with validated error bounds: non-resonant and resonant spectra. *J. Nonlinear Sci.*, 26(4):1055–1095, 2016.
- [37] J. B. van den Berg and J. D. Mireles James. Parameterization of slow-stable manifolds and their invariant vector bundles: theory and numerical implementation. *Discrete Contin. Dyn. Syst.*, 36(9):4637–4664, 2016.
- [38] William D. Kalies, Shane Kepley, and J. D. Mireles James. Analytic continuation of local (un)stable manifolds with rigorous computer assisted error bounds. *SIAM J. Appl. Dyn. Syst.*, 17(1):157–202, 2018.
- [39] Jorge Gonzalez and J. D. Mireles James. High-order parameterization of stable/unstable manifolds for long periodic orbits of maps. *SIAM Journal on Applied Dynamical Systems*, 16(3):1748–1795, 2017. <https://doi.org/10.1137/16M1090041>.
- [40] Chris M. Groothedde and J. D. Mireles James. Parameterization method for unstable manifolds of delay differential equations. *Journal of Computational Dynamics*, pages 1–52, (First online September 2017). doi:10.3934/jcd.2017002.
- [41] Lei Zhang and Rafael de la Llave. Transition state theory with quasi-periodic forcing. *Commun. Nonlinear Sci. Numer. Simul.*, 62:229–243, 2018.
- [42] Stavros Anastassiou, Anastasios Bountis, and Arnd Bäcker. Recent results on the dynamics of higher-dimensional Hénon maps. *Regul. Chaotic Dyn.*, 23(2):161–177, 2018.
- [43] Stavros Anastassiou, Tassos Bountis, and Arnd Bäcker. Homoclinic points of 2D and 4D maps via the parametrization method. *Nonlinearity*, 30(10):3799–3820, 2017.
- [44] Àlex Haro, Marta Canadell, Jordi-Lluís Figueras, Alejandro Luque, and Josep-Maria Mondelo. *The parameterization method for invariant manifolds*, volume 195 of *Applied Mathematical Sciences*. Springer, [Cham], 2016. From rigorous results to effective computations.

- 
- [45] J. D. Mireles James. Validated numerics for equilibria of analytic vector fields: invariant manifolds and connecting orbits. *Proceedings of Symposia in Applied Mathematics*, 74:1–55, 2018.
- [46] Jan Bouwe van den Berg, J. D. Mireles James, Jean-Philippe Lessard, and Konstantin Mischaikow. Rigorous numerics for symmetric connecting orbits: even homoclinics of the Gray-Scott equation. *SIAM J. Math. Anal.*, 43(4):1557–1594, 2011.
- [47] D. Ambrosi, G. Arioli, and H. Koch. A homoclinic solution for excitation waves on a contractile substratum. *SIAM J. Appl. Dyn. Syst.*, 11(4):1533–1542, 2012.
- [48] Gianni Arioli and Hans Koch. Existence and stability of traveling pulse solutions of the FitzHugh-Nagumo equation. *Nonlinear Anal.*, 113:51–70, 2015.
- [49] A. Wittig, M. Berz, J. Grote, K. Makino, and S. Newhouse. Rigorous and accurate enclosure of invariant manifolds on surfaces. *Regul. Chaotic Dyn.*, 15(2-3):107–126, 2010.
- [50] S. Newhouse, J. Palis, and F. Takens. Bifurcations and stability of families of diffeomorphisms. *Inst. Hautes Études Sci. Publ. Math.*, (57):5–71, 1983.
- [51] Jan Bouwe van den Berg, Andréa Deschênes, Jean-Philippe Lessard, and Jason D. Mireles James. Stationary coexistence of hexagons and rolls via rigorous computations. *SIAM J. Appl. Dyn. Syst.*, 14(2):942–979, 2015.
- [52] Daniel Wilczak and Piotr Zgliczynski.  $c^n$ -lohner algorithm. *Scheade Informaticae*, 20:9–46, 2011.
- [53] Daniel Wilczak and Piotr Zgliczynski. Heteroclinic connections between periodic orbits in planar restricted circular three-body problem—a computer assisted proof. *Comm. Math. Phys.*, 234(1):37–75, 2003.
- [54] Daniel Wilczak. Symmetric homoclinic solutions to the periodic orbits in the Michelson system. *Topol. Methods Nonlinear Anal.*, 28(1):155–170, 2006.
- [55] Gianni Arioli and Piotr Zgliczyński. Symbolic dynamics for the Hénon-Heiles Hamiltonian on the critical level. *J. Differential Equations*, 171(1):173–202, 2001.
- [56] Maciej J. Capiński and Anna Wasieczko-Zajac. Geometric proof of strong stable/unstable manifolds with application to the restricted three body problem. *Topol. Methods Nonlinear Anal.*, 46(1):363–399, 2015.
- [57] Maciej J. Capiński. Computer assisted existence proofs of Lyapunov orbits at  $L_2$  and transversal intersections of invariant manifolds in the Jupiter-Sun PCR3BP. *SIAM J. Appl. Dyn. Syst.*, 11(4):1723–1753, 2012.